



HAL
open science

Textural evolution of metallic phases in a convecting magma ocean: A 3D microtomography study

A. Néri, M. Monnereau, J. Guignard, M. Bystricky, C. Tenailliau, B. Duployer, M. J. Toplis, G. Quitté

► To cite this version:

A. Néri, M. Monnereau, J. Guignard, M. Bystricky, C. Tenailliau, et al.. Textural evolution of metallic phases in a convecting magma ocean: A 3D microtomography study. *Physics of the Earth and Planetary Interiors*, 2021, 319, 10.1016/j.pepi.2021.106771 . insu-03672385

HAL Id: insu-03672385

<https://insu.hal.science/insu-03672385>

Submitted on 2 Aug 2023

HAL is a multi-disciplinary open access archive for the deposit and dissemination of scientific research documents, whether they are published or not. The documents may come from teaching and research institutions in France or abroad, or from public or private research centers.

L'archive ouverte pluridisciplinaire **HAL**, est destinée au dépôt et à la diffusion de documents scientifiques de niveau recherche, publiés ou non, émanant des établissements d'enseignement et de recherche français ou étrangers, des laboratoires publics ou privés.



Distributed under a Creative Commons Attribution - NonCommercial 4.0 International License

Textural evolution of metallic phases in a convecting magma ocean: a 3D microtomography study

A. Néria,^{§,*} M. Monnereau^a, J. Guignard^{a,&}, M. Bystricky^a, C. Tenailleau^b, B. Duployer^b, M.J. Toplis^a, G. Quitté^a

^aIRAP, Université de Toulouse, CNRS, CNES, UPS, Toulouse, France

^bCIRIMAT-UMR CNRS 5085, 118 route de Narbonne, 31062 Toulouse cedex 9, France

[§]Now at Bayerisches Geoinstitut, University of Bayreuth, Bayreuth, Germany

[&]Now at CNRS, UMR 6112, Université de Nantes, Laboratoire de Planétologie et Géodynamique, Nantes, France

*Corresponding author, e-mail address: adrien.neri@uni-bayreuth.de

Abstract

The textures of solid and molten metal in the presence of varying fractions of silicate melt at high temperature have been investigated to shed light on differentiation processes occurring in magma oceans formed on rocky bodies of the early solar system. Analogue experiments have been performed in a three-phase system (composed of coexisting metal, forsterite and silicate melt) in both static (1 GPa, 1,723 K) and dynamic (i.e. agitated, at 1 bar, 1,713 K and 1,743 K) conditions. Micro-textures were analyzed with SEM and EBSD techniques, while macro-textures of the metallic phase were analyzed using ex-situ 3D microtomography.

Although all samples exhibit the same micro-scale organization consistent with the minimization of local interfacial energy, their macro-scale textures differ significantly. Static conditions produce metal grains that have shapes close to spherical, corresponding to the state predicted by the grain-scale minimization of interfacial energies. In contrast, under dynamic conditions and in the presence of high silicate melt fractions (≥ 50 vol%), molten metal coalesces to form pools with sizes that are several orders of magnitude larger than those predicted by grain growth mechanisms. Furthermore, in agreement with expectations based upon an interfacial energy budget, images shows that nickel grains, whether solid or molten, do not occur surrounded entirely by silicate melt, but rather in contact with both forsterite crystals and silicate melt, leading to the formation of composite aggregates.

Assuming that a magma ocean has less than 50 vol% of crystals (the upper limit that permits convective motion), thermodynamic calculations indicate that at the necessary temperatures, the

30 metallic subsystem (Fe-Ni-S) of the planetesimal is entirely molten and the silicate residue is only
31 composed of olivine. Convective motions in such a body will drive agitation, promoting the formation of
32 composite aggregates of olivine and molten iron-sulfide, their initial coalescence and subsequent
33 fragmentation. In detail, these composite aggregates have a reduced density contrast with the
34 surrounding silicate melt that reduces their settling velocities compared to pure metal. They also
35 entrain olivine during the downward migration of iron-sulfide pools. Olivine grains concentrate at the
36 surface of the metallic pools, hindering coalesce between pools or with a pre-existing core. An
37 alternative differentiation scenario for core formation is explored in which the simple compaction of
38 partially molten mixtures in the basal non-convecting layer of the magma ocean expels the interstitial
39 silicate melt upward, such that the local fraction of iron-sulfide increases by mass-balance, reaching its
40 percolation threshold and allowing core formation. This process is not only limited to early accreted
41 planetesimals but may also occur in terrestrial bodies.

42 **1. Introduction**

43 Small rocky bodies that accreted within the first 1.5 Myr after the condensation of Calcium-
44 Aluminum-rich Inclusions (CAIs) underwent efficient differentiation leading to a complete separation of
45 metallic and silicate phases, as highlighted by the meteoritic record (Weisberg et al., 2006) and
46 geochemical evidence (e.g. Kruijer et al., 2014). Among these objects are the parent bodies of iron
47 meteorites and the Howardite-Eucrite-Diogenite (HED) clan. Textures and compositions of iron
48 meteorites indicate slow cooling of an entirely molten metallic reservoir (Chabot and Haack, 2006;
49 Goldstein et al., 2009 and references therein). The temperature conditions to fully melt the metallic
50 subsystem point towards a significant degree of melting of the silicate subsystem ($\geq 50\%$). Similarly,
51 the HED clan displays an extremely homogeneous oxygen isotopic composition, which is interpreted
52 as the result of efficient homogenization due to turbulent mixing at high degrees of partial melting, i.e.
53 a global convective magma ocean (Greenwood et al., 2014).

54 Recent efforts have been made to constrain the conditions that allow planetesimals to undergo a
55 magma ocean stage. Unlike planets, the energy source at play in the differentiation of small bodies is
56 not the gravitational energy released during accretion, as this process is negligible for sizes below
57 1000 km. For such “small” bodies, the energy driving differentiation comes from short-lived
58 radionuclides that were accreted along with the body. ^{26}Al and ^{60}Fe are considered to dominate the
59 heat budget in light of their short half-lives (Goswami et al., 2005; Rugel et al., 2009) and their high

60 thermal energy per decay (Castillo-Rogez et al., 2009). Because of their fast decay, the heating
61 potential of a body is much greater for early accretion. Considering these two radionuclides, numerical
62 models predict a wide range of accretion date - radius couple values for which a planetesimal reaches
63 a degree of melting that could have exceeded 50%, thus undergoing a magma ocean stage (e.g.
64 Hevey and Sanders, 2006; Moskowitz and Gaidos, 2011).

65 In a pioneering study, Moskowitz and Gaidos (2011) have shown that bodies accreted within 2 Myr
66 after CAIs and with radii larger than 10 km have the potential to produce a crystal-free magma ocean.
67 However, this study only considered conductive heat transport, while convective motions are much
68 more efficient to dissipate heat, thus decreasing the peak temperature and expanding the range of
69 radius - accretion date in which crystal-bearing magma oceans may occur. Supporting this idea,
70 bodies with radii up to 100 km and accreted as early as 0.1 Myr reach peak temperatures that do not
71 allow more than 80 vol % of melting (Lichtenberg et al., 2019, 2018). When studying the generation of
72 a dynamo by thermally-driven convection in bodies of 500 km in radius and accreted at 0.8 Myr, the
73 recent work of Dodds et al. (2021) found that the peak temperatures of magma oceans do not
74 significantly exceed 1600 K, indicating no more than 50 vol% of melting of the silicates. To summarize
75 these theoretical studies, there appears to be ample room for magma oceans in the early solar
76 system. Although the more recent study of Dodds et al. (2021) suggests that residual crystal fractions
77 remained significant (in the range 20-50 vol%), this range remains sufficiently low to allow efficient
78 convective motion.

79 Under these conditions, metal-silicate differentiation has been proposed to occur through a “rain” of
80 metallic droplets (e.g. Rubie, 2015), a mechanism that seems to be much more efficient than the
81 percolation of an interconnected iron-sulfide melt responsible for the partial differentiation of primitive
82 achondrites (Néri et al., 2019). Considering iron-sulfur globules sinking in a crystal-bearing magma
83 ocean, Taylor (1992) calculated the minimum size of a globule to sink efficiently depending on the
84 degree of melting of the silicates and the planetesimal radius. According to Taylor (1992), for crystal
85 fractions in the range 20-50%, globules have to reach sizes from 1 to 1000 cm for bodies with radii
86 ranging from 250 to 10 km respectively. To reach such sizes from the micrometric metal grains of
87 chondritic material, an efficient growth mechanism is required. Ostwald ripening like grain growth
88 mechanisms have been discussed in magma ocean scenarios (Guignard, 2011; Yoshino and Watson,
89 2005). However, coalescence is also a process of importance in magma oceans, as convective motion

90 is likely to bring metallic particles in contact with each other. To the best of our knowledge,
91 coalescence processes have been poorly addressed in such contexts (Ichikawa et al., 2010).

92 The present study reports the textural evolution of partially molten experimental samples
93 representative of crystal-bearing magma oceans through the use of 3D X-ray Computed
94 microTomography (CT). In previous experimental work (Néri et al., 2019), it was noted that gas
95 bubbles trapped in 1-bar experiments agitated the sample during the experiment, favoring clustering of
96 metallic grains. Similar experiments were conducted here in a three-phase system (forsterite - silicate
97 melt - pure metal) with large and varying silicate melt contents (>30 %), using a 1-bar atmosphere
98 controlled high temperature furnace. Both solid and molten states of metal were investigated to study
99 the effect on coalescence, and bubble-driven agitation is used as a proxy to shed light on the textural
100 evolution of metallic phases in a convecting magma ocean. To fully understand the textures obtained
101 in such dynamic conditions, complementary static experiments on samples devoid of porosity were
102 performed in a piston-cylinder apparatus at 1 GPa. After quenching, the 3D spatial distribution of the
103 metallic phase was characterized ex-situ using computed X-ray microtomography. The micro-textural
104 equilibrium and deformation state of the samples were also investigated with dihedral angle
105 measurements using high resolution Scanning Electron Microscope (SEM) images and EBSD
106 analyses, respectively.

107 **2. Experimental setup**

108 **2.1 Starting material**

109 Samples are synthesized from a mixture of crystalline forsterite (Fo), synthetic silicate melt (Melt)
110 and Nickel metal (Ni). Different mixtures were prepared with varying contents of silicate melt and
111 forsterite, while the absolute metal content was kept constant at 5 vol %. Forsterite and nickel are from
112 commercial powders (Neyco CERAC, Inc., 325 mesh, 99% pure, grain size 0.5-40 μm , and
113 Goodfellow, 99.8% pure, grain size 1-70 μm , respectively). The silicate melt was generated from a
114 silicate glass synthesized from oxide (SiO_2 99.8% – Alfa Aesar, Al_2O_3 99.999% extra pure – Acros)
115 and carbonate (CaCO_3 99+% - Acros, $4(\text{MgCO}_3)\cdot\text{Mg}(\text{OH})_{2.5}(\text{H}_2\text{O})$ - Acros) powders following the
116 procedure described in Néri et al. (2019). The glass composition was chosen in the Anorthite -
117 Diopside - Forsterite (An-Di-Fo) ternary diagram to produce a melt in equilibrium with forsterite at
118 1,713 K and 1 bar or at 1,763 K and 1 GPa (Presnall et al., 1978). This choice allows to vary the

119 relative proportions of forsterite and silicate melt without changing their composition, at a given
120 temperature. Besides, these temperatures are close to the melting point of nickel ($T_m = 1,728$ K at 1
121 bar and $T_m = 1,763$ K at 1 GPa from Strong and Bundy, 1959), thus the temperature can be set above
122 and below the Ni liquidus without changing the composition and absolute proportion of silicate melt
123 significantly.

124 Iron is the most abundant metal in meteorites, rather than nickel. However, the latter is used here
125 as the Nickel - Nickel Oxide buffer occurs at oxygen fugacities ≈ 4 log units above that of the Iron-
126 Wüstite buffer (O'Neill and Pownceby, 1993), a feature that allows a better control of the composition
127 and mineralogy of experimental charges. Previous work on similar systems (Néri et al., 2019) limited
128 amounts of nickel are detected in silicate phases at equilibrium: 2 wt% and 0.6 wt% NiO in forsterite
129 and silicate melt respectively, matching the expected compositions from diffusion and partitioning
130 coefficients (Borisov, 2006; Dingwell et al., 1994; Matzen et al., 2017; Petry et al., 2004).

131 **2.2 Experiments**

132 To constrain the textural evolution of nickel in the presence of large fractions of silicate melt,
133 experiments were conducted in both dynamic and static conditions. As noticed in previous
134 experimental work, bubbles trapped in 1-bar experiments agitate the samples at high temperature,
135 creating a dynamic environment that promotes coalescence. Hence, similar experiments were
136 performed here in a 1-bar controlled atmosphere high temperature furnace (AF). In addition,
137 complementary static experiments were also conducted in a piston-cylinder (PC) at 1 GPa, yielding
138 samples devoid of porosity. Such experiments thus define a steady state that may be compared with
139 results obtained on AF samples. Figure 1 represents the experimental setups used and the
140 experimental conditions are reported in Table 1. Hereafter, PC experiments are referred to as “static”
141 and the AF ones are referred to as “dynamic”.

142 *2.2.1 Dynamic annealing experiments in a 1-bar controlled atmosphere high temperature vertical* 143 *furnace (AF)*

144 A first set of experiments was been performed in a 1-bar controlled atmosphere vertical high
145 temperature furnace (AF). This low pressure is relevant in the case of small bodies with modest radii
146 (no larger than 300 km). To limit the solubility of nickel in silicates during the time of experiment,
147 oxygen fugacity was set to $\log(fO_2) = -8.5$, i.e. 3 orders of magnitude below the Ni-NiO (NNO) buffer

148 ($\Delta_{\text{NNO}} = -3$), using CO and CO₂ gas mixtures. To vary the state of nickel (solid or molten) temperature
149 of the experiment was set either to 1,713 K or 1,743 K, i.e. 15 K below and above the liquidus of
150 nickel. Temperature was measured using an S-type thermocouple (PtRh₁₀ / Pt), ensuring an excellent
151 precision and accuracy of temperature (± 1 K). Samples were suspended in the furnace using the wire
152 loop technique (Figure 1a), as described in Néri et al. (2019). The sample size is typically 5-6 mm³.

153 AF experiments can be divided into two subsets (see Table 1). On the one hand, 24-hour long
154 experiments were run for all compositions (in <Fo:Melt:Ni> vol%: <20:75:5>, <47.5:47.5:5> and
155 <62.5:32.5:5>) to study the resulting textures after this duration. On the other hand, time-series
156 experiments were conducted to follow the kinetics of textural evolution on a single mixture
157 (<20:75:5>). Time-series experiments were first performed below the melting temperature of nickel
158 (1,713 K). In this case, samples were recovered after 1 minute (taken as initial state), 30 minutes, 2
159 hours, 6 hours and 24 hours. A second, another series of experiments was then conducted to study
160 the fate of the coalesced solid nickel grains upon their melting (1,743 K). In this case, samples were
161 equilibrated at 1,713 K for 24 hours (one was recovered), temperature was then increased to 1,743 K
162 and samples were recovered after 30 minutes, 3 hours and 9 hours.

163 The fact that starting materials are powders leads to a significant amount of initial porosity, allowing
164 the formation of bubbles upon melting. These bubble fractions can be determined from 2D and 3D
165 analyses on recovered samples (<20:75:5> time-series) as illustrated in Figure A1. This analysis
166 shows that the gas fraction gradually decreases with time from ≈ 27 vol% after 30 minutes at 1,713 K
167 to 2 vol% after 33 hours (24 hours at 1,713 K then 9 hours at 1,743 K), indicating a slow process of
168 bubbles continuously escaping the sample (see Appendix A.1 for more information).

169 *2.2.2 Static piston-cylinder experiments (PC)*

170 Piston cylinder (PC) experiments have been performed in a 3/4-inch solid medium apparatus at the
171 Laboratoire Magmas et Volcans (LMV, Clermont-Ferrand, France). Experiments were run for 5 hours
172 at 1 GPa and 1,723 K (see Table 1 for compositions), which is 40 K below the melting temperature of
173 Ni at this pressure (Strong and Bundy, 1959). As this temperature is also 40 K lower than the melting
174 temperature of the synthetic glass, the melt composition and the absolute proportions of forsterite and
175 silicate are not subject to strong modifications (Presnall et al., 1978). Although a pressure of 1 GPa is
176 larger than that expected at the center of a 300 km radius body, no significant effects of pressure are
177 expected on the equilibrium textures and on the melting relation between forsterite and silicate melt at

178 values between 1 bar and 1 GPa. Temperature was measured using a type C thermocouple (WRe₅ /
179 WRe₂₆) and controlled using a PID Eurotherm controller. Temperature uncertainties were estimated to
180 be ±5 K during the entire duration of the experiment. The <Fo:Melt:Ni> mixtures were directly
181 enclosed in a graphite capsule, yielding a sample size of about 3 mm³. Although graphite is expected
182 to dissolve into molten nickel, this material has been chosen to fix the oxygen fugacity at reducing
183 conditions and to limit interactions with silicates. MgO tubes and spacers were used to isolate the
184 graphite capsule from the graphite furnace and to align the sample with the hot zone. Pyrex tubes
185 were added on both sides of the graphite furnace, thus limiting shear and stabilizing the assembly. A
186 NaCl cell pressure medium was used to ensure hydrostatic conditions (Figure 1b).

187 **2.3 Analytical techniques**

188 *2.3.1 Ex-situ 3D X-Ray microtomography*

189 Non-destructive 3D X-ray Computed Tomography (CT) was used to characterize the 3D
190 distribution of nickel in recovered samples. Analyses were conducted with operating conditions of 100
191 kV voltage and 130 μA current on a Phoenix/GE Nanotom 180 from the French FERMAT federation
192 (Toulouse, France). A complete scan is composed of 1440 slices taken with an angular resolution of
193 0.25° and a voxel size of 1.5-4 μm. A single slice requires the acquisition of a total of 5 images (750
194 ms per image), out of which the first one is not used (to avoid remanence of previous images on the
195 detector) while the other four are stacked, enhancing the signal to noise ratio. The reconstructed
196 volumes were then obtained by processing the CT scan using the Datosx reconstruction software.

197 *2.3.2 3D data processing*

198 Quantitative data analysis was conducted using Blob3D (Ketcham, 2005). The reconstructed
199 volumes have to be converted into a stack of 8-bit images to be loaded into Blob3D; this conversion
200 was done using ImageJ (Eliceiri et al., 2012; Schindelin et al., 2012). Within the static PC samples,
201 nickel beads are distributed homogeneously, thus Regions of Interest (Rois) of the center of the
202 sample – where the temperature gradient is minimized – were extracted to handle more manageable
203 data-sets (cubes of 500 x 500 x 500 voxels, i.e. ≈0.5 mm³). However, as the metal distribution in the
204 AF reconstructed volumes can be highly heterogeneous, no Rois were defined for these samples and
205 the whole volumes were analyzed to highlight these heterogeneities.

206 Data analysis with Blob3D can be divided into three steps. (1) *Segmentation* - the different phases
207 of interest are identified by assigning a given range of grayscale values to a given phase. For PC
208 experiments, this step was performed by simple thresholding to match the initial proportions, as
209 samples were prepared from precision weighing (each mixture was prepared on 2 g batches using a
210 balance with a precision of 0.1 mg). For AF experiments, the determination of the nickel volume
211 content is not trivial as some is likely to have alloyed with the platinum wires. A reference nickel wire of
212 known diameter was thus placed close to the sample during the CT-scan so that the threshold is
213 adjusted to obtain the right dimension. In this case, simple thresholding refers to assigning all the
214 voxels above a given grayscale threshold value to a phase. Forsterite grains and the silicate glass
215 cannot be identified as separate phases as they have absorption coefficients and densities that are
216 too close to yield distinguishable grayscale values. Hence only two phases were considered in the
217 following: the metal and “silicates”, the latter encompassing both forsterite and silicate melt. The
218 porosity in AF samples was quantified by the use of an additional thresholding step that considered
219 only two components: air and sample (silicates plus nickel). To estimate the error induced by the
220 thresholding step between nickel and silicates, the threshold value was varied by one grayscale level
221 around its reference. Our determined thresholds seem robust as no significant variations of the
222 textural properties of nickel were observed. (2) *Separation* - each individual isolated collection of
223 touching metallic grains (called a “blob”) was identified. In this step, only blobs with volumes larger
224 than 6 voxels were retained for analysis, smaller ones were neglected as they may be considered as
225 detection errors. Due to our small sample sizes, voxel size ranged between 1.5 and 4 μm , which
226 corresponds to lower detection thresholds of 3.4 to 9 μm in terms of sphere-equivalent diameter. The
227 population of grains with sizes lower than 9 μm represents less than 1% of the initial Ni powder. (3)
228 *Extraction* - the desired characteristics of each blob identified in the separation step were then
229 estimated for post-processing analysis. Many parameters can be calculated from ellipsoidal fits, but
230 the shapes of the blobs may deviate strongly from simple geometric shapes (e.g. sphere or ellipsoid).
231 Hence, only volume, surface and Normalized Surface (NS, i.e. the surface of the blob normalized to
232 that of a sphere of equivalent volume; this parameter indicates how much the shape of the blob
233 deviates from sphericity) were extracted.

234 2.3.3 Electronic analysis

235 The micro-scale textures of the samples were characterized using both Field Emission Gun
236 Scanning Electron Microscopy (FEG-SEM) and Electron BackScattered Diffraction (EBSD). This latter
237 technique also provides quantitative information on the deformation processes recorded in crystalline
238 phases due to potential bubble-induced shear in the samples. EBSD was mostly used for the AF time-
239 series experiments with solid nickel, as molten nickel is not likely to record any deformation.
240 Recovered samples were mounted in epoxy resin and polished down to 1/30 μm with colloidal silica.

241 FEG-SEM imaging was performed at the Raimond Castaing Center (Toulouse, France) on a JEOL
242 JSM-7800F Prime FEG-SEM, using a 10 keV accelerating voltage and a 10 nA beam current. EBSD
243 analyses were conducted on a FEG-SEM JEOL JSM 7100F TTLS LV, also at the Raimond Castaing
244 Center (Toulouse, France), with operating conditions of 20 keV accelerating voltage and 18 to 20 nA
245 beam current.

246 **3. Dynamic conditions induced by the presence of gas bubbles within samples**

247 This section describes the effect of agitation on the textural evolution of samples and focuses on
248 time-series experiments using solid nickel. For the sake of clarity and as a thorough description of the
249 effect of agitation does not constitute the main focus of the present study, this section provides a
250 succinct description of the main features of bubble dynamics, a more complete description being
251 available in Appendix sections A.2 and A.3.

252 First of all, it is of note that gravity forces are negligible compared to interfacial energies. The
253 length-scale below which gravity becomes negligible corresponds to the capillary length l_c and is
254 expressed as a function of interfacial energy γ , density ρ and acceleration due to gravity g , following
255 $l_c = \sqrt{\gamma/\rho g}$. Interfacial energies involved here are on the order of 1 J/m², corresponding to a capillary
256 length of about 5 mm, which is greater than the average sample size for either PC or AF experiments
257 (\approx 2-3 mm).

258 In order to understand the conditions that promote agitation, long-duration experiments with
259 different forsterite fractions conducted in agitated conditions (Table 1, AF long run and time-series 1 at
260 24 h) were compared with static runs (Table 1, PC static). Under static conditions (PC samples devoid
261 of porosity), recovered samples show similar textures irrespective of the crystal fraction, with nickel
262 grains homogeneously distributed and with a shape very close to spherical (Figure 2a and 2c). These

263 textures correspond to the state expected from the grain-scale minimization of interfacial energies, as
264 determined by repeated dihedral angle measurements (Néri et al., 2019). However, under agitated
265 conditions (AF samples), textures depend significantly on the crystal fraction. The <62.5:32.5:5>
266 mixture with large crystal fractions shares similar textures with those observed under static conditions
267 (Figure 2a-c). By contrast, mixtures with lower crystal fractions show a heterogeneous spatial
268 distribution of metal grains, that have shapes that deviate largely from a sphere (Figure 2d). Thus,
269 agitation only affects samples with a sufficiently low crystal fraction, controlled by the viscosity of the
270 whole sample (Figure 2d-f). The critical crystal fraction that marks the transition from steady to
271 agitated state can be considered as the maximum packing fraction ϕ_m (e.g. Marsh, 1981; Vigneresse
272 et al., 1996). For crystal fractions larger than ϕ_m , forsterite grains are able to form a rigid skeleton, and
273 bubbles cannot deform the matrix and remain trapped. On the contrary, at lower crystal fractions
274 bubbles are free to move and to alter the textures.

275 The driving force for bubble motion, where possible, is the sudden change in surface caused by
276 coalescence, either between bubbles trapped within the sample, or between a trapped bubble and the
277 atmosphere surrounding the sample, these bubble motions bringing phases in contact with each other.
278 Because the nickel-nickel interfacial energy is one of the lowest (by analogy with iron, Murr, 1975),
279 nickel grains stick together and form large aggregates that adopt the shape of elongated veils as seen
280 on optical images and EBSD fields (Figures 2e,f and A5). On the other hand, the interfacial energy
281 ratios of this system are such that triple junctions between (1) silicate melt-forsterite-nickel, (2) gas-
282 silicate melt-forsterite and (3) gas-silicate melt-nickel are all stable (Laporte and Provost, 2000; Néri et
283 al., 2019; Yao and Mungall, 2020). Even though they may not be the most energetically favorable,
284 these different populations of triple junctions remain, hindering bubble movement and explaining why
285 bubbles find themselves trapped within the samples for long times.

286 **4. Experimental analogue for magma oceans: coalescence of molten nickel** 287 **pools**

288 To investigate the fate of the large metal clusters formed by solid nickel (Figures 2d-f A2f) in the
289 <20:75:5> sample that experienced dynamic conditions, an additional time-series experiment has
290 been conducted at 1 bar, using the same composition but above the melting point of nickel (Table 1,
291 AF time-series 2). In this case, the metal has a lower viscosity and reorganization is enhanced by

292 additional possibilities to minimize interfacial energies. For this experiment, samples were first
293 equilibrated at 1,713 K for 24 h to obtain large solid aggregates as previously observed. Temperature
294 was then increased to 1,743 K, i.e. 15 K above the nickel melting temperature, and samples were
295 quenched at different times (Table 1, Figure 3). Results indicate that upon melting, the coalesced
296 metal clusters that had formed at low temperature break apart above the melting point of metal,
297 modifying significantly metal size distributions. These samples are good analogues for processes
298 occurring in a convective magma ocean.

299 Figure 3a-d and 3e-h show the 3D views of the spatial distribution of nickel blobs and the silicate
300 shell respectively for this time-series experiment; quantitative data of detected blobs are presented in
301 Figure 3i-p. In detail, two types of representations are used. (1) *Normalized Surface (NS)* is plotted as
302 a function of blob volume (Figure 3i-l) - this parameter gives the surface of the detected blobs
303 normalized to that of a sphere of equivalent volume, thus indicating how the shape of the blob
304 deviates from a sphere. To complement this indicator, the wire-equivalent aspect ratio, which
305 corresponds to the aspect ratio of in terms of height to diameter ratio for a cylinder of equivalent NS, is
306 also represented on the right y-axis (Figure 3i-l). For more details on the determination of the wire-
307 equivalent aspect ratio, the reader is referred to Appendix A.4. (2) *Volume fraction distribution* (Figure
308 3m-p) displays the nickel volume fraction in each bin, normalized to the total nickel content of the
309 sample.

310 **4.1 Fragmentation of nickel clusters upon melting**

311 The reference state with solid Ni for this time-series experiment (24 hours with solid Ni)
312 corresponds to the equivalent dynamic sample shown in Figures 2d and A2c,f. The main features of
313 this reference state can be summed up as follows (see Appendix A.2 for more details): (1) the
314 population of the largest grains (in the range 10^5 - $10^8 \mu\text{m}^3$) has large NS and wire-equivalent aspect
315 ratios, indicating shapes that largely deviate from a sphere (Figure 3i), (2) there is a large gap in size
316 between the largest nickel cluster and the rest of the nickel population and (3) this large nickel cluster
317 contains almost 80 vol% of the total nickel within the sample (Figure 3m).

318 After half an hour spent above the Ni liquidus (Figure 3b), aggregates of solid Ni grains break up
319 into many pools (the number of Ni blobs going from 1649 in the solid state to 3721 just after melting)
320 that have spherical shapes, with a wire equivalent aspect ratio that does not exceed ≈ 10 (Figure 3j).
321 Chains of nickel grains probably break apart at places that were previously grain boundaries, as these

322 locations may constitute weak points. This interpretation is supported by the mean volume of blobs
323 that drops by more than one order of magnitude to $3,500 \mu\text{m}^3$ (sphere equivalent radius of $10 \mu\text{m}$
324 instead of $134 \mu\text{m}$ for the initial large-cluster), i.e. approximately the mean grain size of the starting
325 nickel powder. Although the mean pool size has been significantly modified, volume fraction
326 distributions have similar characteristics to those of dynamic samples with solid nickel (Figure 3m-p),
327 showing a gap between the largest blob and the rest of the population.

328 Fragmentation of nickel aggregates at the solid-liquid transition is explained by the spontaneous
329 development of Plateau-Rayleigh instabilities. The pressure along the axis of a liquid thread of
330 average radius r and viscosity μ_i , suspended in an immiscible liquid of viscosity μ_o , is subject to
331 variations caused by changes of its section. The pressure ΔP due to surface tension γ , also called the
332 capillary pressure $\Delta P = \frac{2\gamma}{r}$, varies proportionally as the inverse of the local curvature radius r and
333 therefore tends to transfer fluid from the necks to the bulges, until fragmentation into a series of
334 droplets occurs. This kind of liquid thread segmentation was first been studied theoretically by
335 Tomotika (1936) then experimentally by Stone et al. (1986). The characteristic timescale for changes
336 in the thread shape is $\mu_o r (1 + \mu_i / \mu_o) / \gamma$, which is about one tenth of the time to achieve fragmentation
337 (Stone et al., 1986). For high viscosity contrasts, such as the present experimental system, the
338 dynamics are controlled by the high-viscosity liquid, i.e. the silicate liquid. Taking a silicate melt
339 viscosity on the order of $1 \text{ Pa}\cdot\text{s}$ (estimated from Bottinga and Weill, 1972), the characteristic timescale
340 for breakup is on the order of 10^{-4} s . In other words, fragmentation occurs on time-scales that are
341 certainly no longer than that of nickel melting, so that the situation depicted half an hour after melting
342 of nickel (Figure 3b) is well after this time. Concerning the size of droplets immediately after the
343 aggregate break-up, this parameter is related to the wavelength of the thread varicosities or, in
344 absence of varicosity, to the most unstable wavelength. This latter is theoretically around twice the
345 circumference of the liquid thread, corresponding to droplets twice as large as the thread cross-
346 section. These theoretical predictions match the observations in our recovered samples: before nickel
347 melting (24 h with solid Ni) the thread cross section is about $10 \mu\text{m}$ (between 6 and $15 \mu\text{m}$, as
348 measured on the EBSD fields shown in Figures 2f and A5), which is half the size of the mean nickel
349 droplet diameter of $20 \mu\text{m}$, measured in the sample recovered 30 min after crossing the Ni melting
350 temperature (Figure 3n).

351 **4.2 Fast coalescence of nickel pools**

352 As the time spent above the Ni liquidus temperature increases, nickel pools coalesce, decreasing
353 the number of detected blobs down to 56 after 9 hours (qualitatively seen in Figure 3b-d), and
354 increasing the mean volume, up to 487,300 μm^3 after 9 hours (i.e. a sphere equivalent radius of 50
355 μm). Contrary to nickel clustering in the solid state, NS values show that molten nickel pools preserve
356 their spherical shapes over time (Figure 3j-l). The volume fraction distribution (Figure 3n-p) indicates
357 that the largest blob remains separated from the rest of the population and jumps from gathering 20
358 vol% of nickel after 0.5 hours (Figure 3n) above the liquidus to 40 vol% after 3 hours (Figure 3o). This
359 value seems to be an upper threshold as it remains constant even after 9 hours (Figure 3p).
360 Interestingly, the number of large blobs increases with time and represents a growing fraction of the
361 total nickel. For instance, 9 hours after Ni melting (Figure 3p), the 7 largest blobs (in the range 10^6 - 10^7
362 μm^3) represent more than 90 vol% of the total nickel. The odd shape of the volume fraction distribution
363 after 9 hours is likely due to a lack of statistics (56 detected blobs). Differences in the absolute
364 maximum grain sizes also reflect the different sample sizes.

365 The irregular clusters of nickel are disrupted upon melting due to the development of Plateau-
366 Rayleigh instabilities, but the newly-formed spherical pools are able to coalesce and to grow on
367 extremely short timescales. Indeed, if only Ostwald ripening pool growth mechanisms are considered,
368 metallic pools are expected to grow only up to 12 μm in radius (at 1743 K, Yoshino and Watson, 2005)
369 during the time of experiment, while coalescence mechanisms in our experiments resulted in a mean
370 pool size of 50 μm in radius. Hence, coalescence is much more efficient than growth through ripening,
371 as it reduces the number of grains and increases the mean volume by two orders of magnitude in a
372 matter of a few hours. Molten nickel pools are able to preserve their spherical shapes as they are not
373 affected by shear.

374 **4.3 Formation of forsterite-nickel composite aggregates**

375 Unfortunately, the 3D volumes do not reveal the phase relations between forsterite, silicate melt
376 and molten nickel as both solid and liquid silicate phases share highly similar X-ray absorption
377 contrasts. On the other hand, when looking at *ex-situ* optical images of the time-series experiments
378 with molten Ni, an interesting feature arises: nickel pools are far from being entirely wetted by silicate
379 melt (Figure 4). Irrespective of the time spent above the nickel liquidus, a large number of them has a
380 large number of forsterite grains on their surface, thus forming composite aggregates. For small times

381 spent above the nickel liquidus (0.5 h and 3 h, Figure 4a and 4b), the proportions of free nickel grains
382 and that of forsterite crystals attached to the surface of a nickel pool seem quite variable along a 2D
383 plane. However, as coalescence proceeds, nickel pool size exceeds that of forsterite grains (Figure
384 4c). Although nickel pools are scarce and hard to find along a 2D plane, this shift in size seemingly
385 causes the nickel pools to gather a uniform “layer” of crystals on their surface.

386 The formation of such composite aggregates can be understood in terms of interfacial energies.
387 For the silicate melt to fully wet forsterite grains and nickel pools, all forsterite-nickel interfaces would
388 have to be replaced by two new interfaces: a forsterite-silicate melt interface and a nickel-silicate melt
389 one. In terms of interfacial energy balance, such a condition would require that $\gamma_{Fo-Ni} > \gamma_{Melt-Fo} +$
390 $\gamma_{Melt-Ni}$, in terms of interfacial energies. In the case of solid Ni and taking the interfacial energy ratios
391 determined by Néri et al. (2019), this inequality is not respected and such forsterite-nickel-silicate melt
392 triple junctions are stable, even though they may not be the most energetically favorable. Due to the
393 dynamics within our samples, nickel pools and forsterite crystals are constantly brought in contact with
394 each other, ensuring the formation and persistence of such composite aggregates.

395 Iron is the most abundant metallic phase present in meteorites rather than nickel, thus it is
396 important to assess if nickel and iron behave in similar or different ways. In this respect, an electrical
397 conductivity study (Bagdassarov et al., 2009) and a recent microtomography study focusing on the
398 interconnectivity of Fe-S melts in well-equilibrated matrixes (Solferino et al., 2020) both indicate that
399 Fe-bearing melts are not as wetting as previously thought (e.g. Yoshino et al., 2003), with a newly
400 determined interconnection threshold of ≈ 18 vol%. In general, the addition of sulfur to a pure metallic
401 phase within a silicate matrix decreases its dihedral angle and thus its interfacial energy (e.g. Holzheid
402 et al., 2000). As such, our experiments thus constitute a “worst case scenario” with a large nickel-
403 olivine interfacial energy that reduces the efficiency of aggregate formation compared to Fe-Ni-S
404 natural melts. These arguments all go in favor of the formation of composite metal-olivine aggregates
405 in natural Fe-dominated magma oceans. The presence of such aggregates is essential to take into
406 consideration as the time- and length-scales of their segregation may be very different from that of
407 simple metal droplets, as explored in the next sections.

408 **5. Implications for metal-silicate differentiation in magma oceans**

409 Metal-silicate separation in magma-ocean is usually considered under the paradigm of iron rain in
410 a fully molten silicate bath (e.g. Rubie et al., 2003). While this approach is justified in the context of a
411 magma ocean left behind by a giant impact, such as that from which the Moon originated, it loses
412 relevance in the case of the primordial evolution of small bodies, where the degree of melting may be
413 lower and therefore the settling of metallic droplets may occur in a crystal mush rather than in pure
414 silicate liquid.

415 **5.1 Petrology and minimum crystal fraction in magma oceans**

416 The petrology and differentiation processes associated with of magma oceans on small bodies are
417 poorly known. Although there is little information on the precursor materials of planetesimals that
418 underwent a magma ocean stage, study of the asteroid Vesta indicates that ordinary chondrites and
419 more precisely H chondrites seem to be a major component (e.g. Toplis et al., 2013). An H chondrite
420 precursor composition (Wasson and Kallemeyn, 1988) is thus assumed in the following. To provide
421 preliminary insight into parent-body differentiation, equilibrium melting (i.e. without melt extraction) of
422 H chondrite precursor material at 1 bar and along the Iron-Wüstite buffer was simulated using the
423 “rhyolite-melts” thermodynamic calculator (Asimow and Ghiorso, 1998; Ghiorso and Gualda, 2015;
424 Ghiorso and Sack, 1995; Gualda et al., 2012). The melting curve of the metallic subsystem was also
425 calculated at 1 bar, assuming equilibrium (Buono and Walker, 2011) and a H chondrite precursor
426 (Guignard and Toplis, 2015; Wasson and Kallemeyn, 1988). The melting curves for both the silicate
427 and metallic subsystems as a function of temperature are illustrated in Figure 5 as a function of
428 temperature.

429 As discussed above, a degree of melting of 50-80 vol% seems to be an upper limit for magma
430 oceans (Dodds et al., 2021; Lichtenberg et al., 2019), while the lower limit is most likely buffered by
431 viscosity: viscosity, as this parameter has to be low enough to allow convective motions to operate.
432 Indeed, at a critical crystal fraction ϕ_m , the rheology of a mixture of liquid and suspended solid
433 particles drastically changes and is either controlled by the solid ($\phi > \phi_m$) or the liquid ($\phi < \phi_m$). The
434 value of ϕ_m depends on the shape and size of crystals, but literature data bracket values between 0.4
435 and 0.74, with a value of ≈ 0.6 for geologically relevant materials (Costa et al., 2009; Marsh, 1981;
436 Scott and Kohlstedt, 2006). We note that such values are supported by our experimental results based

437 on the efficiency of agitation. To further narrow down this range of rheological thresholds, terrestrial
438 basaltic magma chambers can be taken as analogue systems. The crystallinity of basaltic lavas
439 produced in such contexts have been extensively studied by Marsh (1981) who showed that most of
440 these materials have phenocryst contents lower than 50-55 vol%. Using a semi-empirical approach, it
441 is also possible to calculate the maximum packing fraction depending on the aspect ratio of grains
442 (Mader et al., 2013). Assuming an aspect ratio of 1 for equant olivine grains, one would find $\phi_m =$
443 0.55, consistent with the maximum crystal fraction determined from natural samples. Hence, a value of
444 0.5 used here as the lower bound for melt content for formation of a magma ocean, marking the onset
445 of convection.

446 Combining these considerations with the calculations shown in Figure 5, magma oceans would be
447 formed on bodies that exceed $\approx 1,700$ K, the temperature at which 50 vol% of the silicates are molten
448 (dashed black line). At such temperatures, the metallic subsystem is fully molten and thus would form
449 spherical coalesced pools. Furthermore, the silicate residue is largely dominated by olivine (≈ 85 vol%)
450 with a minor amount of orthopyroxene (≈ 15 vol%), a fraction that decreases rapidly to zero only at
451 1,730 K. Magma oceans should thus be considered as a mixture of silicate melt, spherical Fe-FeS
452 pools and floating olivine crystals (plus minor orthopyroxene). Due to convective motion, these metallic
453 pools are likely to be brought into contact and coalesce, ensuring their fast and efficient growth,
454 similarly to our experiments. However, the determined interfacial energy budget also predicts the
455 formation of olivine - Fe-FeS aggregates that may decrease the efficiency of coalescence and
456 differentiation. Both effects are discussed below to assess the efficiency of the iron-sulfide rain as a
457 differentiation mechanism in crystal-bearing magma oceans.

458 **5.2 Coalescence, breakup and settling**

459 We begin by considering the end-member scenario of metal-silicate separation taking place
460 through the “iron-rain” in a fully liquid silicate bath. For this exercise, metal droplets representing 10%
461 of the volume (assuming an H chondrite precursor material (Guignard and Toplis, 2015)) and therefore
462 constituting a dilute suspension, were considered. In this case, the settling conditions of the dense
463 particles depend on their relative Stokes velocity with respect to the mean convective ones. As the
464 Stokes velocity is proportional to the square of the particle size, increases in sizes due to coalescence
465 may play a major role in triggering settling. However, coalescence is limited by the decrease in the
466 probability of collision, which decreases as the number of particles falls (due to particle growth), and

467 fragmentation (or breakup) also counteracts the coalescence process. Fragmentation occurs when the
468 shape of the metallic pools deviates from that of a sphere, i.e. when forces tending to deform the
469 surface – the viscous drag, the inertial forces – overcome surface tensions that tend to keep it
470 spherical and whose strength is inversely proportional to the curvature radius. As a result, the
471 competition between coalescence and fragmentation, may lead to an equilibrium size before settling.
472 Ichikawa et al. (2010) simulated iron rain in a fully molten magma ocean. They investigated the
473 evolution of either a single large blob breaking up into smaller globules or the coalescence of several
474 small blobs. In both cases, the system reaches a steady state within less than a minute with a mean
475 pool size of ≈ 15 mm. Overall, these simulations indicate that the equilibrium between coalescence and
476 fragmentation processes occurs on a very short timescale in a fully molten magma ocean.

477 While these insights are of interest, in a magma ocean formed early in the thermal evolution of
478 small rocky bodies in the early solar system, the presence of crystals will have a first-order impact on
479 coalescence and settling, potentially invalidating conclusions based on consideration of a simple two-
480 phase mixture. Firstly, the presence of crystals increases the number of particles to the point where
481 the medium can no longer be considered as a dilute suspension, and settling velocities are likely to be
482 hindered. Besides, the interfacial energy budget suggests that the residual silicate crystals are
483 attached to the surface of the iron-sulfide pools, producing a shielding effect that can alter the
484 probability of coalescence or breakup. For example, two colliding aggregates may simply bounce off
485 each other if their relative velocity is too low, or if the phase that touch are solid (i.e. olivine).
486 Fragmentation may also be enhanced. Indirect evidence for such complexity provided by our
487 experimental results which show that the largest metallic blobs do not exceed 40 vol% of the total
488 nickel within the sample and that this maximum size (sphere equivalent radii on the order of a few
489 hundred microns) is reached within a few hours (Figure 4) – a much longer time than the minutes
490 predicted by Ichikawa et al. (2010) for crystal-free magma oceans. The apparent end of coalescence
491 observed in our experiment can be interpreted either as the result of an equilibrium due to a decrease
492 in the population of metallic blobs, or as the result of olivine crystals at the surface of the blobs
493 hindering coalescence, and most likely as a combination of these two effects. In any case, this
494 shielding seems to reduce the maximum size that the iron-sulfide droplets are able to reach. Given the
495 diversity and complexity of the coalescence/fragmentation mechanisms in a simple two-phase system,
496 it seems too uncertain to discuss this shielding effect further.

497 On the other hand, the number densities of metal droplets and olivine crystals as a function of their
 498 respective sizes may be used to provide insights into the ability of crystals to attach to metal pools and
 499 form aggregates. The mechanisms of droplet and crystal growth (coalescence and Ostwald ripening,
 500 respectively) have very different timescales. Indeed, coalescence occurs on the order of a few minutes
 501 in the numerical simulations of Ichikawa et al. (2010) or of a few hours in our experiments, while
 502 thousands of years are required for silicate crystals to reach millimeter sizes (Guignard, 2011), as
 503 observed in pallasites. We may thus consider that the coalescence of iron-sulfide droplets occurs in
 504 a population of olivine crystals that remains stable in number and size. The direct consequence is that
 505 during coalescence, the number of metal droplets decreases as the cube of their size and therefore
 506 the number of surrounding silicate crystals increases at the same rate, which leads to a significant
 507 decrease in the probability of the drops colliding with each other.

508 To take this analysis one step further, let us assume a magma ocean resulting from the partial
 509 melting of silicates where the fraction of silicate melt is x , $(1 - x)$ being the fraction of residual solid
 510 silicate, and containing 10 vol% of liquid metal. If the metal is distributed in a population of drops
 511 whose average diameter is d_m , their number per unit volume is $n_m = 0.6/(\pi d_m^3)$. In the same way, the
 512 number of olivine crystals of size d_o is $n_o = 5.4(1 - x)/(\pi d_o^3)$. Now, if we assume that each metallic
 513 drop is covered by olivine crystals forming a dense shield of thickness d_o , the number of olivine grains
 514 possibly attached can be approximated by $n_{ao} = n_m \times 6d_m^2/d_o^2$. The factor of 6 is obtained by
 515 calculating the volume of the crystal shield as the surface area of the metal drop times d_o , an
 516 approximation only valid when $d_m \gg d_o$. This is a good estimation of the number of crystals that may
 517 actually stick to the surface of a sphere of diameter d_m . If $d_m = d_o$, the maximum number of spheres
 518 bonding a central sphere of the same size is 12, instead of 6 in our approximation, while the exact
 519 calculus of the volume of a shell of thickness d_m is 26 times the droplet volume. The actual number of
 520 crystals attached to the metal surface cannot be larger than the total number of crystals, but it can be
 521 lower, so that remaining olivine crystals are free to move between aggregates. Their number density is
 522 $n_{fo} = n_o - \min(n_o, n_{ao})$. From this simple consideration of particle populations, it follows that the ratio
 523 of the number of olivine crystals to the number of metal droplets, n_o/n_m , varies as d_m^3/d_o^3 , while the
 524 ratio of the number of olivine crystals possibly attached to a metal droplet to the number of metal
 525 droplets n_{so}/n_m varies as d_m^2/d_o^2 . Therefore, beyond the threshold $d_m/d_o \geq 2/3(1 - x)$, the surfaces

526 of the metallic droplets are entirely covered by olivine crystals and the number of free crystals
527 increases as the cube of the metal droplet size.

528 The evolution of the number of metal droplets, of free olivine crystals and of attached olivine grains
529 is plotted in Figure 6. The two curves (full lines and dashed lines) correspond to degrees of partial
530 melting of 50 vol% (full lines) and 80 vol% (dashed lines), both bounding the range of crystal fractions
531 obtained from numerical simulations of magma oceans (Dodds et al., 2021; Lichtenberg et al., 2019).
532 Sketches in Figure 6 represent the different configurations expected for different size ratios.
533 Thresholds corresponding to entirely shielded surfaces of iron-sulfide pools and to the presence of
534 free crystals are for $d_m/d_o = 4/3$ and $10/3$ respectively. Figure 6 shows that the ratio number of free
535 crystals to iron-sulfide pools increases from 100 to 1000 for size ratios of 3 to 6 when the degree of
536 melting is 50%. At 80%, this range is covered for size ratios of 5 to 10. Coalescence of the aggregates
537 will likely slow down above a certain density of free crystals. Determining a threshold is certainly
538 difficult, but one thing we note is that the size ratio at which coalescence ceases is about 5 when the
539 proportion of liquid corresponds to a degree of fusion of 80% (Figure 4c). This indicates that
540 aggregates cannot easily grow beyond a size ratio of a few units once the threshold d_m/d_o is reached.
541 As mentioned earlier, once the iron-sulfide pool is entirely shielded by olivine crystals, its probability of
542 coalescing with surrounding ones is very low. Besides, at this size ratio of 5 in the case of 80% of
543 partial melt, two thirds of olivine crystals adhere to metal drops and are likely to settle together. The
544 same proportion is also observed for a size ratio of 2 in the 50% melting degree case. The possibility
545 that the aggregates sediment more rapidly and thus separately from the free olivine crystals is another
546 question that is difficult to answer. This is certainly easier for large degrees of silicate partial melting
547 rather than at the onset of convection in magma oceans.

548 In light of the discussion above, it appears that the behaviour of a three-phase system shows
549 important differences compared to the two-phase system commonly adopted to treat metal-silicate
550 separation in a magma ocean through iron-rain. It is clear that the presence of crystals hinders the
551 coalescence of metal drops and the separation of metal from silicate. The possibility that metal and
552 silicate crystals settle together at the beginning of the magma ocean (i.e. in the vicinity of 50% of
553 partial melting) must be taken into account. This eventuality is discussed in the next section.

554 **5.3 Implications for the differentiation of crystal bearing magma oceans: a new differentiation**
555 **pathway?**

556 As argued above, iron-sulfide pools do not settle alone but have attached olivine crystals that
557 prevent efficient core formation through an iron-rain scenario. In other words, iron-sulfide pools cannot
558 coalesce to form a core. There is thus a need to rethink differentiation pathways for crystal-bearing
559 magma oceans. A better understanding of the onset and evolution of magma oceans in planetesimals
560 is required, with, for instance, accurate determinations of magma ocean lifetimes, or the behavior of
561 convection with significant crystal fractions. Modeling efforts are required in these directions.
562 Preliminary efforts are made here to propose an alternative differentiation pathway to the iron-rain
563 scenario, as illustrated schematically in Figure 7.

564 In previous studies, the relevance of iron-rain differentiation in the presence of residual crystals has
565 been addressed by comparing the settling velocity of molten iron-sulfide pools to that of the ascending
566 convection currents (e.g. Taylor, 1992). Although highly interesting in the case of composite
567 aggregates, this exercise cannot be performed here because the dynamic conditions of this system
568 (coalescence, fragmentation, phase separation and phase aggregation) preclude a precise mass
569 balance of the aggregates. In addition, this calculation would only investigate the aggregate buoyancy
570 in ascending convection currents, while the ascending velocity is null at the bottom of convection cells,
571 creating areas of efficient settling and accumulation (Figure 7a,b). As the crystal fraction is locally
572 increased, and most likely above the rheological threshold, convection cannot proceed in such
573 accumulation areas. The height of the convecting magma ocean is thus decreased, leaving a column
574 of “crystal mush” (> 50 vol% olivine + silicate melt + metal). This column will undergo compaction once
575 its height is sufficient, expelling the less dense silicate melt upward (Figure 7b). Considering a simple
576 mass balance, the removal of at least 50 vol% of the silicates increases the iron sulfide melt content to
577 at least ≈ 20 vol%. At such volume fractions, the Fe-FeS melt is able to form a persistent
578 interconnected network (Bagdassarov et al., 2009; Néri et al., 2020; Solferino et al., 2020) and thus to
579 percolate downward, forming the metallic core (Figure 7c). Percolation hysteresis and the relatively
580 low trapping thresholds evidenced by Ghanbarzadeh et al. (2017) ensures efficient drainage of most
581 of the iron-sulfide melt. Compaction of a planetesimal at the end of life of the magma ocean thus
582 constitutes an efficient alternative differentiation pathway for planetesimals that underwent a crystal-
583 bearing magma ocean stage. It is of note that this differentiation pathway is not limited to early

584 accreted small bodies, and may have also taken place at the end of life of magma oceans on
585 terrestrial bodies.

586 **Conclusion**

587 The textural evolution of a metallic phase in the presence of large quantities of silicate melt has
588 been studied through experiments conducted in both a piston cylinder apparatus and an atmospheric
589 furnace. In the former, conditions remained static, while in the latter, gas bubbles escaping the sample
590 agitated the medium and offered dynamical conditions. Micro- and macro-scales textures have been
591 compared and discussed in the context of magma oceans in planetesimals. The following conclusions
592 can be drawn:

593 (1) In dynamic experiments, gas bubbles agitate the samples when they coalesce with the
594 surrounding atmosphere. Due to the interfacial energy budget of this system and bubble motions,
595 nickel blobs are brought in contact with each other and subsequently form elongated veils if solid, or
596 large spherical pools if molten. Whether nickel is solid or molten, agitation is able to form clusters of
597 metal that gather a significant fraction of the total nickel on relatively short timescales. In such silicate
598 melt-rich systems, coalescence processes are much more efficient than growth driven by Ostwald
599 ripening, and seem to control the growth kinetics.

600 (2) All samples show the same micro-textural equilibrium but different macro-textural properties.
601 Samples from static experiments contain spherical metallic blobs irrespective of the silicate melt
602 content, corresponding to the state predicted by the grain-scale minimization of interfacial energies.
603 On the contrary, textures of solid nickel in the dynamic experiments depend on the crystal fraction, i.e.
604 on the efficiency of agitation, strong agitation favoring the formation of large irregular nickel clusters.
605 Melting these clusters causes their disruption into spherical pools on very short time-scales.

606 (3) Defining a magma ocean as a partially molten system bearing less than 50 vol% of residual
607 crystals (to allow convective motion), we show that at these conditions, the iron-sulfide subsystem is
608 fully molten, and the silicate residue is largely dominated by olivine. Composite aggregates of olivine
609 and molten iron-sulfide pool are able to form due to the interfacial energy budget. The presence of
610 olivine grains on the surface of the iron-sulfide pools affects the coalescence-fragmentation
611 processes. Metallic pools are able to coalesce and grow until their size is such that their surface
612 become entirely covered by olivine crystals. Once this has happened, iron-sulfide pools have a

613 reduced probability of encountering surrounding pools and $\approx 2/3$ of the residual olivine crystals are not
614 free in the silicate melt but are rather attached to the pools.

615 (4) As iron-sulfide pools settle together with olivine grains, they cannot simply coalesce with a pre-
616 existing core. In crystal-bearing magma oceans formation of a metallic core will not be as efficient as
617 suggested by the iron-rain scenario derived from consideration of fully molten magma oceans. A new
618 differentiation scenario is proposed in which, at the end of life of the magma ocean, the compaction of
619 the planetesimal expels the silicate melt upward, locally increasing the metal fraction above its
620 interconnection threshold and thus allowing its efficient percolation downward.

621 **Acknowledgements**

622 We wish to thank Ken Koga and Didier Laporte (LMV, Université Clermont-Auvergne, Clermont-
623 Ferrand, France) for helpful discussions on piston-cylinder assemblies and experiments, and
624 Stéphane Le Blond du Plouy and Arnaud Proietti (Centre Raimond Castaing, Toulouse, France) for
625 SEM imaging and EBSD analyses, respectively. Authors also acknowledge Alexander Rother
626 (Bayerisches Geoinstitut, Bayreuth, Germany) for emergency sample preparation. This work is part of
627 the PALLAS project funded by the ANR (grant ANR-14-CE33-006-01 to G. Quitté); authors also thank
628 the Université Paul Sabatier for its contribution to the PhD grant to A. Néri.

629

630 **Table 1:** Starting phase proportions, experimental conditions and 3D X-Ray microtomography
631 resolutions of the different experiments. AF is for the 1-bar atmosphere controlled high temperature
632 furnace experiments and PC is for the piston-cylinder experiment. In the voxel size column, N.D.
633 refers to experiments that were not analyzed with 3D X-Ray microtomography, but with EBSD.
634 Superscript * denotes temperature conditions where nickel is molten.

<Fo:Melt:Ni> (vol%)	Set up	Experiment type	Pressure (GPa)	Temperature (K)	Time	Voxel size (μm)
<20:75:5>	AF	Time-series 1	10 ⁻⁴	1,713	0.02 h	N.D.
<20:75:5>	AF	Time-series 1	10 ⁻⁴	1,713	0.5 h	N.D.
<20:75:5>	AF	Time-series 1	10 ⁻⁴	1,713	2 h	N.D.
<20:75:5>	AF	Time-series 1	10 ⁻⁴	1,713	6 h	N.D.
<20:75:5>	AF	Time-series 1	10 ⁻⁴	1,713	24 h	1.54 μm
<20:75:5>	AF	Time-series 2	10 ⁻⁴	1,713 then 1,743*	24 h then 0.5 h	1.54 μm
<20:75:5>	AF	Time-series 2	10 ⁻⁴	1,713 then 1,743*	24 h then 3 h	2.56 μm
<20:75:5>	AF	Time-series 2	10 ⁻⁴	1,713 then 1,743*	24 h then 9 h	1.54 μm
<47.5:47.5:5>	AF	Long run	10 ⁻⁴	1,713*	24 h	4.25 μm
<62.5:32.5:5>	AF	Long run	10 ⁻⁴	1,713*	24 h	3.76 μm
<20:75:5>	PC	Static	1	1,753	5 h	1.23 μm
<47.5:47.5:5>	PC	Static	1	1,753	5 h	1.50 μm
<62.5:32.5:5>	PC	Static	1	1,753	5 h	1.50 μm

635

636

637 **Figure 1:** Schemes showing the assemblies used for the experiments conducted in this study. (a) 1-
638 atmosphere controlled high temperature furnace assembly. Samples are suspended in the hot-zone of
639 the furnace thanks to an alumina rod in which platinum wires are bended to form hooks, allowing to
640 place the wire loops. Temperature is monitored with a type S thermocouple (± 1 K). (b) Piston-cylinder
641 assembly. Samples are encapsulated in graphite and placed in the hot-zone of the furnace with MgO
642 spacers. Temperature is monitored and controlled using a type C thermocouple (± 5 K).

643 **Figure 2:** (a-d) 3D images of the nickel spatial distribution for the <62.5:32.5:5> (a-b) and <20:75:5>
644 (c-d) recovered samples in both PC (top row) and AF (bottom row) experiments. The five largest blobs
645 are colored while the rest is in semi-transparent gray. For the steady PC experiments and the
646 <62.5:32.5:5> dynamic one, nickel blobs are homogenously distributed, although the presence of
647 bubbles slightly affects the nickel distribution, as evidenced by regions of low blob density. This
648 comparison indicates that bubble stirring was not be efficient in the presence of large silicate crystal
649 contents, in opposition to the samples with larger silicate melt contents, which show large blobs that
650 widely deviate from a spherical shape. These large blobs are seen not only on 3D images but also on
651 2D optical images (e). The green rectangle delimits the analyzed EBSD field. EBSD analyses indicate
652 that the large nickel blobs are composed of aggregated solid grains (thick black lines outline the grain
653 boundaries). These individual grains are largely deformed, as seen by the high density of sub-grain
654 boundaries (thin black line) and are elongated, highlighting the efficiency of stirring.

655 **Figure 3:** (a-d) Textural evolution of nickel and (e-h) silicate shells for the time-series experiments
656 across its melting temperature for the <20:75:5> composition in dynamic conditions. The five largest
657 blobs of each sample are represented following the same color code as in Figure 3, the rest of the
658 detected nickel blobs are represented in semitransparent gray. The state just before nickel melting (a)
659 corresponds to the image shown in Figure 3f. Quantitative data extracted on Ni blobs are also
660 represented on this figure: (i-l) NS populations as a function of blob volume and (m-p) volume fraction
661 distributions. Soon after melting (0.5 hours, b, f, j and n), the previously formed solid nickel network
662 has been completely disrupted into smaller metallic blobs that have spherical shapes, the largest one
663 gathers up to 10 vol% of the total nickel of the sample. The mean blob size corresponds to the mean
664 value of the starting nickel powder. With time and due to agitation, the metallic blobs grow by
665 coalescence and form larger spheres. As a consequence, the mean volume drastically increases by a

666 factor of 140 between 0.5 and 9 h, but the largest blob seems not to be able to cluster more than 40
667 vol% of the total nickel within the sample. The number of blobs also decreases and the volume
668 fraction distributions show a large gap in size between the largest blobs and the rest of the distribution.

669 **Figure 4:** Optical images of recovered samples from the <20:75:5> time-series experiments in
670 dynamic conditions with molten nickel. These pictures indicate that due to the interfacial energy
671 budget of this three-phase system, nickel grains are not fully surrounded by silicate melt but rather are
672 able to attach to nickel pools, thus forming composite aggregates. With time and increasing nickel pool
673 size, more forsterite grains are able to remain attached to the surface of the pool.

674 **Figure 5:** Modal proportions of the silicate and metallic subsystems as a function of temperature. The
675 dashed vertical line indicates the temperature at which 50 vol% of melting is achieved for the silicates.
676 Melting of the metallic subsystem is calculated using data of Buono and Walker (2011) at 1 bar and
677 assuming a H chondrite precursor material (7 wt% S, Wasson and Kallemeyn, 1988) that bears 10
678 vol% of iron-rich phases (Guignard and Toplis, 2015). The equilibrium melting of the silicate
679 subsystem is calculated using Rhyolite-Melts (Asimow and Ghiorso, 1998; Ghiorso and Gualda, 2015;
680 Ghiorso and Sack, 1995; Gualda et al., 2012), at 1 bar, along the Iron-Wüstite buffer and also
681 assuming a H chondrite composition (Wasson and Kallemeyn, 1988). These results indicate that the
682 metallic subsystem is fully molten upon the onset of convection in a magma ocean, i.e. when ≈ 50 vol%
683 of the silicates are molten. In this case, the silicate residue is mainly composed of olivine with minor
684 contents of orthopyroxene that vanishes rapidly. As olivine remain over a wide range of temperature,
685 agitation is likely to bring metallic pools and residual crystals together, forming composite aggregates.

686 **Figure 6:** Populations of metal drops and olivine crystals as function of their respective size ratio
687 d_m/d_o . The number of particles distributing a certain volume percentage of a material decreases as
688 the cube of the particle size. The blue curves show the ratio between the number of metal drops and
689 the number of olivine crystals per unit volume of magma containing 10% of molten metal and 90% of
690 partially molten silicates at 50% (plain line) and 80% (dashed line). The orange line indicates the
691 relative number of olivine crystals possibly attached to the surface of metal drop n_{ao} . If this number is
692 less than the number of existing olivine crystals, there remain free crystals not attached to metal drop.
693 Their number n_{fo} is plotted by the green curves. Three sketches at the bottom of the graph illustrate
694 the situations corresponding to d_m/d_o size ratios of 0.3, 1 and 3. Depending on the degree of partial

695 melting, iron-sulfide pools become fully shielded for different size ratios. At this point, because the
696 spatial density of iron-sulfide is largely decreased and because of the olivine casing, molten pools
697 have a drastically decreased on encounter probability, limiting the maximum size they could reach.

698 **Figure 7:** Schematic drawing of the proposed differentiation pathway for crystal-bearing magma
699 oceans. (a.) Convective motions bring iron-sulfide pools (gray spheres) and residual olivine grains
700 (green crystals) together such that they are able to form composite aggregates. These aggregates are
701 able to settle at the bottom of convection cells, i.e. in locations where the ascending current velocity is
702 null, creating areas of accumulation of iron-sulfide melt, olivine crystals and interstitial silicate melt. (b.)
703 As the local crystal fraction at the bottom of convection cells is larger than the maximum packing
704 fraction, convection stops and compaction is able to proceed, thus expelling the less dense silicate
705 melt upward. (c.) The removal of the interstitial silicate melt allows the iron-sulfide melt fraction to
706 exceed its interconnection threshold, fostering its efficient percolation downward and core formation.

707

708 **Appendix**

709 **A.1 Evolution of gas fraction within samples**

710 To investigate the evolution of the gas fraction within our samples and make sure that the observed
711 textures are indeed comparable, both 2D optical images and 3D volumes were used. From these, a
712 similar thresholding procedure was applied: two components were considered and thresholded, (1)
713 “air” and (2) “silicates” that comprise silicate melt, forsterite crystals and nickel grains. Then the
714 volume of each detected phase was normalized to the sum of these two components, finally giving the
715 relative proportion of gas bubbles trapped. Results as a function of time for the <20:75:5> time-series
716 experiments with both solid and molten nickel are shown in Figure A1.

717 The sample recovered 0.5 h after the beginning of the experiment shows a large porosity fraction
718 of about 25 vol%. Porosity within samples then decreases with time, first rapidly with a decrease of
719 almost half within 6 h and then more slowly with a loss of $\approx 2\%$ over 18 h. Upon melting of the nickel
720 after spending 24 h with solid Ni, a new sudden decrease of porosity is observed and is most likely
721 driven by the surface change that occurred during fragmentation of the large nickel aggregates.
722 Variations in the slope of the porosity fraction as a function of time indicate that the stirring conditions
723 within the samples are not constant and are gradually less efficient with time, as less bubbles are
724 present. However, samples follow the exact same trend with time, thus arguing that textures can be
725 meaningfully compared between samples to track a time evolution. The porosity fraction in the sample
726 recovered after 24 h with solid nickel was determined using both 2D and 3D data and show a variation
727 of only 2 vol% in the determined porosity. Such a small variation between the two techniques ensures
728 that the comparison between the two is reliable.

729 **A.2 The effect of silicate melt content on the efficiency of agitation**

730 A first series of experiments has been run in order to investigate the effect of silicate melt fraction
731 on textural evolution both in static (PC) and dynamic (AF) conditions. Comparison between these
732 different environments further highlights the effect of stirring (caused by bubbles), since pressurized
733 static experiments are devoid of gas bubbles and are thus indicative of textures resulting from the
734 minimization of interfacial energies alone.

735 Figure A2 shows 3D images of the solid metal distribution in the different samples and the silicate
736 shell for the AF experiments. Quantitative data for nickel blobs extracted with Blob3D (Ketcham, 2005)

737 are shown in Figure A3. To correct for the effect of different experimental run duration and help
738 graphical comparison, the x-axis of the volume fraction distribution corresponds to the volume of the
739 blobs normalized to the mean blob volume.

740 The results from static experiments (PC) show a homogeneous spatial distribution of spherical
741 nickel blobs regardless of the silicate melt content: the five largest blobs are not readily apparent as
742 they blend into the rest of the mass (Figure A2a-c). Nickel blobs in the <20:75:5> sample could have
743 been expected to settle at the bottom of the sample, due to the high silicate melt content. However,
744 interfacial energy forces overcome gravitational ones in our experimental charges, thus it would
745 appear that a composite network of nickel and forsterite is formed and maintains the nickel particles
746 suspended over the time of experiment. The variations of normalized surface (NS) show similar trends
747 irrespective of the silicate melt content, with NS values no larger than 5 and wire equivalent aspect
748 ratios that do not exceed 2-3, thus indicating blobs with shapes close to spherical (Figure A3a-c, black
749 dots). Volume fraction distributions are narrow and similar for all static samples (Figure A3d-f, black
750 step curves), with mean volumes of $\approx 2,000 \mu\text{m}^3$ (i.e. a sphere equivalent radius of $8 \mu\text{m}$,
751 corresponding to the mean initial grain size), and grain volumes that range from 10 to $200,000 \mu\text{m}^3$
752 (i.e. sphere equivalent radii that range from $1.3 \mu\text{m}$ to $36 \mu\text{m}$). Variations in the number of blobs
753 detected, especially for the <20:75:5> sample, arise from the different voxel sizes of acquisition (see
754 Table 1). Overall, a normal distribution shape (lognormal in log scale) is preserved, which is expected
755 from the initial grain size distribution. These static experiments exhibit meso-textures that perfectly
756 match the micro-scale observations and can thus be taken as an equilibrium reference state that was
757 not affected by any kind of agitation.

758 In contrast, samples that experienced dynamic conditions show a heterogeneous spatial
759 distribution of nickel, with textures that vary as a function of the silicate melt content (Figures A2 and
760 A3). The presence of gas bubbles is shown by voids in the spatial density of Ni, representation of the
761 silicate envelope (Figure A2d-i) and simply optical images of the samples (Figure A4). Although the
762 <62.5:32.5:5> sample contains a significant fraction of porosity, the characteristics of the blobs are
763 very similar to those of samples that did not experience agitation, with a NS population and volume
764 fraction distribution that can be almost superimposed (e.g. Figure A3a and A3d). However, slight
765 differences are apparent: the population of large blobs of the AF sample (10^5 - $10^6 \mu\text{m}^3$) exhibits greater
766 wire equivalent aspect ratios (in the range 10-100) and its maximum ($10^6 \mu\text{m}^3$, i.e. $120 \mu\text{m}$ sphere

767 equivalent diameter) and mean (15,000 μm^3 , i.e. 30 μm sphere equivalent diameter) grain sizes are
768 one order of magnitude higher than at static conditions (Figure A3a and A3d). These two features
769 reflect a minor clustering of metallic blobs due to thermal expansion of gas bubbles trapped when
770 temperature increased. Dynamic samples with larger silicate melt contents (<47.5:47.5:5> and <20:75
771 5> mixtures) have textures that largely differ from other samples, with solid metallic blobs locally
772 clustered in the form of irregular aggregates, as indicated by the five largest blobs in Figure A2e and
773 A2f. The irregularity of blobs is best seen on NS populations (Figure A3b and A3c, red dots), with NS
774 values larger than 5 and the largest blobs having wire equivalent aspect ratios up to 1,000. Volume
775 fraction distributions have a unique characteristic, they show a large gap in size between the largest
776 blob and the rest of the distribution (Figure A3e and A3f, red step curves). The largest blob of a
777 dynamic experiment is a solid network formed of multiple grains (see Appendix section A.3) that
778 clusters a significant amount of the total nickel: 20 and 80 vol% respectively for the <47.5:47.5:5> and
779 <20:75:5> mixtures. For comparison, the largest blobs of PC experiments represent less than 1 vol%
780 of the total nickel (Figure A3d-f, black step curves). All these properties highlight a mechanism of
781 efficient clustering of nickel particles, Ni grains sticking to each other due to surface tensions.

782 An interesting feature of the AF experimental series is that the <62.5:32.5:5> sample does not
783 display nickel clusters that are as large as the <47.5:47.5:5> or <20:75:5> samples (Figures A2 and
784 A3). This is interpreted to be the consequence of different crystal fractions that control the degree of
785 agitation. Indeed, the crystal-rich <62.5:32.5:5> sample is likely to have a touching framework of solid
786 silicates that impede gas bubbles from moving freely within the sample, explaining their irregular
787 shapes (Figure A4). On the contrary, in the melt-rich <20:75:5> sample, the silicate matrix has a
788 rheology primarily controlled by the silicate melt, that is sufficiently weak that it does not disturb the
789 free motion of bubbles within the sample, favoring efficient agitation. The efficiency of agitation thus
790 comes down to a question of viscosity of the crystal - melt mixtures. The rheology of even a simple
791 binary system composed of solid particles suspended in a liquid is complex and not yet fully
792 understood, thus we will not attempt to quantify the details of a mixture of crystals bathed in two
793 immiscible fluids. However, in general terms, considering a forsterite - silicate melt mixture, the effect
794 of crystal fraction (ϕ) on viscosity for binary mixtures is typically addressed through the notion of a
795 rheological threshold (ϕ_m , e.g. Marsh, 1981; Vigneresse et al., 1996), i.e. the crystal fraction at which
796 all crystals are in contact with one another. For $\phi > \phi_m$, a rigid silicate framework is formed with a high

797 viscosity, roughly that of forsterite, which precludes any deformation or shear due to bubble motion.
798 On the other hand, if the crystal fraction decreases below ϕ_m , then viscosity decreases rapidly and
799 remains sufficiently low for gas bubbles to stir the sample. The <20:75:5> mixture seems well below
800 ϕ_m as agitation is highly efficient and homogeneous within the sample. In turn, the <47.5:47.5:5>
801 mixture appears to be close to the ϕ_m value of this system as bubbles do not have a homogeneous
802 effect. Finally, the crystal fraction of the <62.5:32.5:5> mixture seems above ϕ_m as bubbles did not
803 affect the metal textures, explaining the irregular shapes of gas bubbles that were preserved over the
804 duration of the experiment (Figures A2f and A4). The rheological threshold of the present experimental
805 system thus lies between 47.5 and 62.5 vol% of crystals.

806 Taken together, these results indicate that for identical starting mixtures, the gas bubbles trapped
807 in the silicate matrix of AF samples have agitated the system and caused the observed clustering of
808 solid metallic grains, while PC samples devoid of porosity do not show such features. This agitation
809 seems extremely efficient to create local concentrations of solid metal grains on short timescales and
810 to preserve the irregular textures over the duration of the experiment. For bubble stirring to be
811 efficient, a significant fraction of silicate melt has to be present (≈ 50 vol%), although this agitation is
812 likely to be heterogeneous in the <47.5:47.5:5> sample as demonstrated by a fraction of large grains
813 with spherical shapes (Figure A3b).

814 **A.3 Bubble-driven agitation evidenced by time-series experiments**

815 A second AF time-series experiments were conducted to study the microtextural evolution of solid
816 nickel (<20:75:5> mixture at 1,713 K). These experiments were observed by optical imaging before
817 being analyzed with FEG-SEM imaging coupled with EBSD to evaluate the deformation that affected
818 the samples.

819 Optical images are displayed in Figure A5a-d and show the distribution of the different phases over
820 the time of experiment. The presence of gas bubbles within the samples requires explanation but most
821 likely comes from the inherent residual porosity in the sample prepared from ground powders. A
822 number of striking features further arise when examining these images: (1) gas bubbles remain
823 trapped in the sample, (2) most of these bubbles are not only surrounded by silicate melt but also
824 remain in contact with forsterite and/or nickel grains, (3) these grains are always primarily in contact
825 with the silicate melt, (4) some gas bubbles are surrounded by nickel grains and (5) nickel forms

826 elongated chains with only silicate melt on one side and a concentration of forsterite crystals on the
827 other (Figure A5a-d red arrows).

828 Features (1), (2) and (3) can be understood by the grain-scale minimization of interfacial energies
829 alone as surface tensions remain the prevailing force at such micro-scales. In these experimental
830 charges, the geometry and phase relations are thus dictated by interfacial energies, whose relative
831 importance can be assessed by repeated dihedral angle measurements. An accurate quantification of
832 such angles at forsterite - silicate melt - nickel triple junctions on similar three-phase systems with
833 solid Ni shows no dependence on the experiment duration or on the relative proportions of the
834 different phases (Néri et al., 2019), and reveals an extremely low dihedral angle value for silicate melt
835 ($\approx 23^\circ$) and high values for forsterite ($\approx 161^\circ$) and nickel grains ($\approx 176^\circ$). The interfacial energies of the
836 system that can thus be sorted as follows: $\gamma_{Melt-Fo} < \gamma_{Melt-Ni} < \gamma_{Fo-Ni}$ (Néri et al., 2019). Although the
837 interfacial energy between forsterite and nickel is the largest of the system, nickel beads are
838 systematically observed in contact with forsterite crystals as the energy condition for the silicate melt
839 to fully wet forsterite crystals and nickel grains, $\gamma_{Fo-Ni} > \gamma_{Melt-Fo} + \gamma_{Melt-Ni}$, is not reached.
840 Considering gas - silicate melt - forsterite and gas - silicate melt - nickel triple junctions, similar
841 inequalities could be written for γ_{Gas-Fo} and γ_{Gas-Ni} with respect to the silicate melt. Based on Yao and
842 Mungall (2020) and references therein, and Laporte and Provost (2000), this condition is again not
843 reached, preserving the existence of forsterite - silicate melt - gas and forsterite - nickel - gas triple
844 junctions, thus giving rise to features (1) and (2). Silicate melt, however, wets most of the surface of
845 the gas bubbles as it is the phase of lowest interfacial energy.

846 The remaining features (4) and (5) cannot be explained on the basis of interfacial energies alone;
847 they also require a dynamic environment. Indeed, nickel forms large structures within the first 0.5 hour
848 of the experiment (Figure A5a), which are preserved over the time of experiment (Figure A5b-d). The
849 grain-scale minimization of interfacial energy should theoretically lead nickel grains to form spheres,
850 but the observed textures largely deviate from that, highlighting a dynamic equilibrium that prevents
851 the system from reaching the minimum energy state. This dynamic equilibrium is generated by the
852 stirring driven by bubble movement within the sample: not only the number of bubbles decreases with
853 increasing run duration, but their size also evolves with the relative proportion of small bubbles
854 seemingly increasing (Figure A5a-d). Bubbles growth is then expected over time, either by Ostwald
855 ripening or by coalescence. The former mechanism is driven by the variation from one bubble to

856 another of the difference in pressure between the inside and outside of a bubble. This pressure
857 difference, the Laplace or capillary pressure (ΔP), is related to the bubble radius (r) as follows: $\Delta P =$
858 $\frac{2\gamma}{r}$, so that the pressure in small bubbles is higher than in the large ones, favoring the dissolution of the
859 gas contained in small bubbles and its exsolution towards the large ones. On the other hand,
860 coalescence is a spontaneous phenomenon because the surface area of two bubbles, and therefore
861 the energy stored in them, is always greater than that of the coalesced bubble. However, this process
862 involves the rupture of the bubble envelope, which is all the more difficult when the bubble is small.
863 Hence coalescence of bubbles within the sample is favored for the largest ones. Besides, the surface
864 of the sample is also an interface between the silicate melt and a gas, with a radius of curvature that is
865 much larger than that of any bubbles it may contain. Thus, the probability of coalescence, i.e. that of a
866 bubble escaping the sample, is maximal for a large bubble in contact with the atmosphere of the
867 furnace. When this happens, there is an abrupt change in the sample-atmosphere interface that
868 induces a release of energy, further dissipated by stirring of the sample. A video of an experiment
869 carried out in the International Space Station, i.e. in microgravity, with a sparkling cachet introduced
870 into a water bubble nicely illustrates this dynamic (https://www.youtube.com/watch?v=bKk_7NIKY3Y).

871 The stirring of the sample induces new coalescence of bubbles, but also leads to nickel grains to
872 stick together. While Ni has the highest interfacial energy with the other phases of the system, the
873 surface energy between two nickel grains is extremely low (by analogy with iron, Murr, 1975), so that
874 two nickel grains brought in contact will not separate easily. Proof of this efficient sticking is provided
875 by analysis of the EBSD images which shows that grain deformation dominates over grain separation.
876 Color-coded EBSD images are displayed in Figure A5e-h (EBSD fields correspond to the green
877 rectangles in Figure A5a-d), with forsterite in green and nickel in red. Thick black lines indicate grain
878 boundaries while the thin ones indicate sub-grain boundaries. The delimitation of grain boundaries
879 clearly indicates that the large Ni structures are composed of an agglomeration of elongated solid
880 nickel grains. Maps of local misorientation are shown in Figure A5i-l, and indicate that, unlike forsterite
881 crystals, nickel grains are affected by significant local misorientation (up to 5°) recorded early during
882 the time of experiment and preserved through time. Within these grains, regions affected by a high
883 misorientation angle correspond to regions with a high density of sub-grain boundaries (Figure A5e-h).
884 Thus, nickel grains undergo a high degree of shearing instead of separating by the agitation process
885 described earlier. This interpretation is supported by the evolution of aspect ratios with time displayed

886 in Figure A3m-p for both forsterite crystals (green) and nickel grains (red), with the forsterite grains
 887 becoming more rounded, while nickel grains are increasingly elongated. Indeed, aspect ratios of
 888 forsterite slightly decrease toward a value of 1, while those of nickel significantly increase with time.
 889 After 24 hours, only 40 vol% of the nickel grains maintain a low aspect ratio, increasing the mean
 890 value to 2.7. Consequences of these low interfacial energies and strong grain boundaries are the
 891 formation of chains of nickel grains that are associated with the movement of gas bubbles. Some
 892 bubbles can thus find themselves completely surrounded by nickel, explaining feature (4), while the
 893 nickel aggregates form large veils that act as nets and collect forsterite grains on one side when they
 894 are dragged, forming feature (5).

895 To summarize, the preparation of the sample and the 1-bar high temperature furnace set-up allow
 896 a significant fraction of porosity to be present during the time of experiment. These bubbles affect the
 897 textural evolution by stirring the sample when they escape at the surface of the sample. This agitation
 898 brings nickel grains in contact with each other, forming of large aggregates or veils due to the low Ni-
 899 Ni interfacial energy. When these structures are entrained by gas bubbles, nickel grains are sheared
 900 and elongated.

901 **A.4 Determination of the wire-equivalent aspect ratio**

902 The wire-equivalent aspect ratio of a blob corresponds to the aspect ratio $n = h/d$, in terms of
 903 height (h) to diameter (d) ratio, of an elongated cylinder of equivalent NS. The normalized surface
 904 (NS), or sphere-normalized surface-to-volume ratio, compares the dimensionless surface-to-volume
 905 ratio (SV) of a 3D object to that of a sphere. In general, one can consider $SV = \sqrt{S^3/V^2}$, which would
 906 give $\sqrt{36\pi}$ for a sphere. To compare the SV value of a cylinder, its surface S and volume V have to be
 907 expressed as a function of its aspect ratio:

$$908 \quad S = \pi d^2 \left(\frac{2n+1}{2} \right), \quad (\text{A.1})$$

$$909 \quad V = \frac{\pi}{4} n d^3, \quad (\text{A.2})$$

910 which finally gives the following relation for the normalized surface of a cylinder:

$$911 \quad NS = \frac{2}{3n} \left(\frac{2n+1}{2} \right)^{3/2}. \quad (\text{A.3})$$

912 In theory, equation A.3 has two solutions, larger or lower than one. Since elongated cylinders are
913 considered, n is to be larger than one by definition. However, the wire equivalent aspect ratio of a blob
914 is not directly calculated, the NS of a cylinder of a given aspect ratio is rather calculated. This trick
915 allows to show the correspondence between NS and wire-equivalent aspect ratio on a secondary y-
916 axis.
917

918 **Figure A1:** Evolution of porosity as a function of time. for the <20:75:5> time-series experiments.
919 Temperature was kept at 1,713 K for 24 hours before being increased to 1,743 K, i.e. 15 K below and
920 above the nickel liquidus respectively. Green dots represent samples with solid nickel and the red
921 ones are for liquid nickel. Squares indicate the porosity fraction detected on 2D slices and triangles the
922 porosity fraction detected from 3D volumes. Overall, the porosity fraction decreases with time. The
923 trend indicates a drastic decrease of porosity within 6 hours, but does not evolve much until 24 hours
924 with solid nickel. Upon melting, there is a rupture in the slope with again a strong decrease in porosity.
925 Most likely, the immediate change in nickel surface upon fragmentation triggers further agitation that
926 helps gas bubbles to escape the sample. It is of note that the porosity estimates after 24 hours with
927 solid nickel are slightly different depending on the 2D or 3D analysis. This difference is, however, of
928 only 2 vol%, thus comparison between the two methods remains reliable. All these observations
929 indicate a gradual loss of porosity with time driven by surface changes within the sample.

930 **Figure A2:** Textures comparison of solid nickel (5 vol% in all samples) between dynamic (AF, a-c for
931 the nickel and d-f for the silicate shell) and static (PC, g-i) experiments with increasing silicate melt
932 contents to the right. The five largest blobs of each samples appear in color and highlight the major
933 differences in sizes and shapes between the samples, while the rest of the nickel is represented in
934 semi-transparent gray. From first to fifth largest: red, orange, purple, blue and green. These 3D X-ray
935 microtomography images show that samples from static experiments have spherical nickel blobs no
936 matter the silicate melt content. The sample from dynamic experiments with 32.5 vol% of silicate melt
937 show textures quite similar to those of static samples. However, dynamic samples with a high
938 proportion of silicate melt (75 vol% and 47.5 vol%) host large clusters of nickel grains that have
939 irregular shapes. Agitation within these samples is most likely what drove this clustering, as static
940 samples with the exact same compositions do not show this feature. The presence of bubbles is
941 evidenced by the presence of voids when representing the silicate shell.

942 **Figure A3:** Comparison of the quantitative data extracted from the 3D volumes of static (black) and
943 dynamic (red) experiments. Differences in nickel textures are quantified using the Normalized Surface
944 (NS, surface of the blob normalized to that of a sphere of equivalent volume, an indicator of the
945 sphericity of the blob) as a function of blob volume (a-c) and the volume distributions normalized to the
946 mean volume (d-f). NS populations show that, for static experiments, nickel blobs have spherical

947 shapes irrespective of the silicate melt content. On the opposite, the shape of nickel blobs in the
948 dynamic experiments are more irregular in samples containing high fraction of silicate melt (b and c),
949 and closer to spheres for lower amounts of silicate melt (a). Volume distributions of these samples
950 show that the nickel volume fraction of the largest blob also depends on the silicate melt content,
951 ranging from ≈ 1 % for low contents (d) to 80 % for the largest silicate melt content (e). Again, static
952 experiments show a completely different behavior with their largest blobs that represent ≈ 1 vol% of the
953 total nickel, no matter the silicate melt fraction. These distributions are narrower than those for
954 dynamic experiments with high silicate melt contents (e and f), and perfectly matched to the
955 experiment with a low silicate melt fraction (d). These features highlight the efficiency of nickel
956 gathering nickel in dynamic experiments.

957 **Figure A4:** Optical maps of samples that remained under dynamic conditions below the nickel solidus
958 for 24 h, with increasing silicate melt content from left to right. Such pictures show that bubbles remain
959 in the samples even after a relatively long time in the presence of silicate melt. Below 50 vol% of
960 crystals, the spatial density of bubbles within the sample is relatively low and they are nicely rounded,
961 while with larger crystal contents and due to the formation of rigid skeleton of forsterite, bubbles have
962 irregular shapes and are unable to escape the sample over time.

963 **Figure A5:** Optical images, EBSD fields and results of the $\langle 20:75:5 \rangle$ ($\langle \text{Fo}:\text{Melt}:\text{Ni} \rangle$ vol%) AF time-
964 series experiments with solid Ni (1,713 K). Run durations are distributed column-wise, with increasing
965 time from 0.5 h (left) to 24 h (right). Optical images of the recovered samples are shown on the first
966 row (a-d). The large metallic disks correspond to the platinum wire of the loop. Red arrows indicate
967 nickel veils with mostly olivine on one side and only silicate melt on the other side. Green rectangles
968 show the analyzed EBSD fields. (e-h) Phase identification of the analyzed surfaces, with nickel in red
969 and forsterite in green. Silicate melt and air bubbles are represented in black, the distinction between
970 the two is best seen on the optical images. Grain boundaries appear in thick black lines while sub-
971 grain boundaries in thin black lines. Nickel seems to be clustered quite rapidly, with the formation of
972 2D solid aggregates as soon as 0.5 hours of experiment, highlighting the efficiency of gathering upon
973 agitation. (i-l) Local misorientation maps, with low misorientation angles in blue and high
974 misorientation angles in red. Forsterite crystals have misorientation angles close to zero while those of
975 the nickel go up to 5° . Grains have elongated shapes, highlighting that agitation drags and stretches

976 them, causing the observed misorientation. (m-p) Distributions showing the evolution of aspect ratios
977 of forsterite and nickel with time, with forsterite in green and nickel in red. Dashed lines denote the
978 average aspect ratio of a phase. With time, forsterite grains tend become more and more rounded,
979 with aspect ratios that decrease toward a value of 1. In opposition, nickel grains have shapes that
980 become more and more elongated until it reaches an average aspect ratio of 2.7 after 24 hours, which
981 supports that nickel textures are the result of the agitation.

982

983 **References**

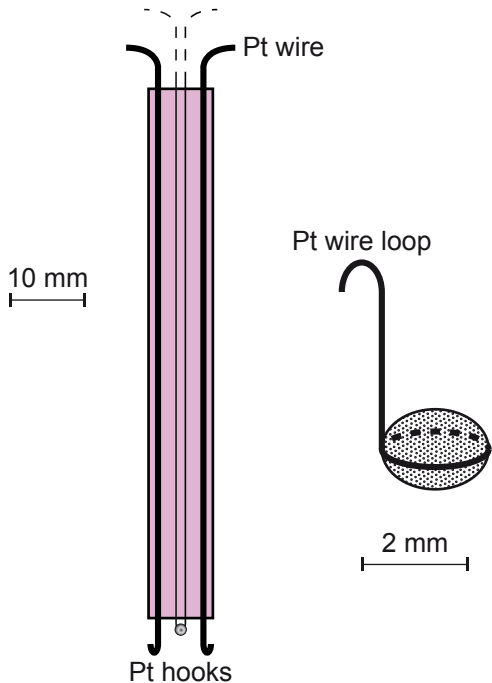
- 984 Asimow, P.D., Ghiorso, M.S., 1998. Algorithmic modifications extending MELTS to calculate
 985 subsolidus phase relations. *Am. Mineral.* 83, 1127–1132. [https://doi.org/10.2138/am-1998-9-](https://doi.org/10.2138/am-1998-9-1022)
 986 1022
- 987 Bagdassarov, N., Golabek, G.J., Solferino, G., Schmidt, M.W., 2009. Constraints on the Fe-S melt
 988 connectivity in mantle silicates from electrical impedance measurements. *Phys. Earth Planet.*
 989 *Inter.* 177, 139–146. <https://doi.org/10.1016/j.pepi.2009.08.003>
- 990 Borisov, A.A., 2006. Experimental study of the effect of SiO₂ on Ni solubility in silicate melts. *Petrology*
 991 14, 530–539. <https://doi.org/10.1134/S0869591106060026>
- 992 Bottinga, Y., Weill, D.F., 1972. The viscosity of magmatic silicate liquids; a model calculation. *Am. J.*
 993 *Sci.* 272, 438–475. <https://doi.org/10.2475/ajs.272.5.438>
- 994 Buono, A.S., Walker, D., 2011. The Fe-rich liquidus in the Fe–FeS system from 1bar to 10GPa.
 995 *Geochim. Cosmochim. Acta* 75, 2072–2087. <https://doi.org/10.1016/j.gca.2011.01.030>
- 996 Castillo-Rogez, J., Johnson, T. V., Lee, M.H., Turner, N.J., Matson, D.L., Lunine, J., 2009. 26Al decay:
 997 Heat production and a revised age for Iapetus. *Icarus* 204, 658–662.
 998 <https://doi.org/10.1016/j.icarus.2009.07.025>
- 999 Chabot, N.L., Haack, H., 2006. Evolution of Asteroidal Cores, in: *Meteorites and the Early Solar*
 1000 *System II*. University of Arizona Press, pp. 747–771.
- 1001 Costa, A., Caricchi, L., Bagdassarov, N., 2009. A model for the rheology of particle-bearing
 1002 suspensions and partially molten rocks. *Geochemistry, Geophys. Geosystems* 10, 1–13.
 1003 <https://doi.org/10.1029/2008GC002138>
- 1004 Dingwell, D.B., O'Neill, H.S.C., Ertel, W., Spettel, B., 1994. The solubility and oxidation state of nickel
 1005 in silicate melt at low oxygen fugacities: Results using a mechanically assisted equilibration
 1006 technique. *Geochim. Cosmochim. Acta* 58, 1967–1974. [https://doi.org/10.1016/0016-](https://doi.org/10.1016/0016-7037(94)90428-6)
 1007 7037(94)90428-6
- 1008 Dodds, K.H., Bryson, J.F.J., Neufeld, J.A., Harrison, R.J., 2021. The Thermal Evolution of
 1009 Planetesimals During Accretion and Differentiation: Consequences for Dynamo Generation by
 1010 Thermally-Driven Convection. *J. Geophys. Res. Planets* 126, 1–31.
 1011 <https://doi.org/10.1029/2020JE006704>
- 1012 Eliceiri, K., Schneider, C.A., Rasband, W.S., Eliceiri, K.W., 2012. NIH Image to ImageJ : 25 years of
 1013 image analysis. *Nat. Methods* 9, 671–675. <https://doi.org/10.1038/nmeth.2089>
- 1014 Ghanbarzadeh, S., Hesse, M.A., Prodanović, M., 2017. Percolative core formation in planetesimals
 1015 enabled by hysteresis in metal connectivity. *Proc. Natl. Acad. Sci.* 114, 13406–13411.
 1016 <https://doi.org/10.1073/pnas.1707580114>
- 1017 Ghiorso, M.S., Gualda, G.A.R., 2015. An H₂O–CO₂ mixed fluid saturation model compatible with
 1018 rhyolite-MELTS. *Contrib. to Mineral. Petrol.* 169, 53. <https://doi.org/10.1007/s00410-015-1141-8>
- 1019 Ghiorso, M.S., Sack, R.O., 1995. Chemical mass transfer in magmatic processes IV. A revised and
 1020 internally consistent thermodynamic model for the interpolation and extrapolation of liquid-solid
 1021 equilibria in magmatic systems at elevated temperatures and pressures. *Contrib. to Mineral.*
 1022 *Petrol.* 119, 197–212. <https://doi.org/10.1007/BF00307281>
- 1023 Goldstein, J.I., Scott, E.R.D., Chabot, N.L., 2009. Iron meteorites: Crystallization, thermal history,
 1024 parent bodies, and origin. *Chemie der Erde* 69, 293–325.
 1025 <https://doi.org/10.1016/j.chemer.2009.01.002>
- 1026 Goswami, J.N., Marhas, K.K., Chaussidon, M., Gounelle, M., Meyer, B.S., 2005. Origin of Short-lived
 1027 Radionuclides in the Early Solar System, in: Krot, A. ~N., Scott, E. ~R. ~D., Reipurth, B. (Eds.),
 1028 *Chondrites and the Protoplanetary Disk*, *Astronomical Society of the Pacific Conference Series*.
 1029 p. 485.
- 1030 Greenwood, R.C., Barrat, J.-A., Yamaguchi, A., Franchi, I.A., Scott, E.R.D., Bottke, W.F., Gibson,
 1031 J.M., 2014. The oxygen isotope composition of diogenites: Evidence for early global melting on a
 1032 single, compositionally diverse, HED parent body. *Earth Planet. Sci. Lett.* 390, 165–174.
 1033 <https://doi.org/10.1016/j.epsl.2013.12.011>

- 1034 Gualda, G.A.R., Ghiorso, M.S., Lemons, R. V., Carley, T.L., 2012. Rhyolite-MELTS: a Modified
1035 Calibration of MELTS Optimized for Silica-rich, Fluid-bearing Magmatic Systems. *J. Petrol.* 53,
1036 875–890. <https://doi.org/10.1093/petrology/egr080>
- 1037 Guignard, J., 2011. Caractérisation texturale des assemblages Métal-Silicate lors de la différenciation
1038 des planétésimaux : Etude de météorites & Approche expérimentale. Université Toulouse III Paul
1039 Sabatier.
- 1040 Guignard, J., Toplis, M.J., 2015. Textural properties of iron-rich phases in H ordinary chondrites and
1041 quantitative links to the degree of thermal metamorphism. *Geochim. Cosmochim. Acta* 149, 46–
1042 63. <https://doi.org/10.1016/j.gca.2014.11.006>
- 1043 Hevey, P.J., Sanders, I.S., 2006. A model for planetesimal meltdown by 26 Al and its implications for
1044 meteorite parent bodies. *Meteorit. Planet. Sci.* 41, 95–106. [https://doi.org/10.1111/j.1945-
1045 5100.2006.tb00195.x](https://doi.org/10.1111/j.1945-5100.2006.tb00195.x)
- 1046 Holzheid, A., Schmitz, M.D., Grove, T.L., 2000. Textural equilibria of iron sulfide liquids in partly
1047 molten silicate aggregates and their relevance to core formation scenarios. *J. Geophys. Res.*
1048 *Solid Earth* 105, 13555–13567. <https://doi.org/10.1029/2000JB900046>
- 1049 Ichikawa, H., Labrosse, S., Kurita, K., 2010. Direct numerical simulation of an iron rain in the magma
1050 ocean. *J. Geophys. Res.* 115, 1–12. <https://doi.org/10.1029/2009jb006427>
- 1051 Ketcham, R.A., 2005. Computational methods for quantitative analysis of three-dimensional features
1052 in geological specimens. *Geosphere* 1, 32. <https://doi.org/10.1130/GES00001.1>
- 1053 Kruijjer, T.S., Touboul, M., Fischer-Godde, M., Bermingham, K.R., Walker, R.J., Kleine, T., 2014.
1054 Protracted core formation and rapid accretion of protoplanets. *Science* (80-). 344, 1150–1154.
1055 <https://doi.org/10.1126/science.1251766>
- 1056 Laporte, D., Provost, A., 2000. The Grain-Scale Distribution of Silicate, Carbonate and Metallosulfide
1057 Partial Melts: a Review of Theory and Experiments, in: Bagdassarov, N., Laporte, D., Thompson,
1058 A.B. (Eds.), *Physics and Chemistry of Partially Molten Rocks*. Springer Netherlands, pp. 93–140.
1059 https://doi.org/10.1007/978-94-011-4016-4_4
- 1060 Lichtenberg, T., Golabek, G.J., Dullemond, C.P., Schönbachler, M., Gerya, T. V., Meyer, M.R., 2018.
1061 Impact splash chondrule formation during planetesimal recycling. *Icarus* 302, 27–43.
1062 <https://doi.org/10.1016/j.icarus.2017.11.004>
- 1063 Lichtenberg, T., Keller, T., Katz, R.F., Golabek, G.J., Gerya, T. V., 2019. Magma ascent in
1064 planetesimals: Control by grain size. *Earth Planet. Sci. Lett.* 507, 154–165.
1065 <https://doi.org/10.1016/j.epsl.2018.11.034>
- 1066 Mader, H.M., Llewellyn, E.W., Mueller, S.P., 2013. The rheology of two-phase magmas: A review and
1067 analysis. *J. Volcanol. Geotherm. Res.* 257, 135–158.
1068 <https://doi.org/10.1016/j.jvolgeores.2013.02.014>
- 1069 Marsh, B.D., 1981. On the crystallinity, probability of occurrence, and rheology of lava and magma.
1070 *Contrib. to Mineral. Petrol.* 78, 85–98. <https://doi.org/10.1007/BF00371146>
- 1071 Matzen, A.K., Baker, M.B., Beckett, J.R., Wood, B.J., Stolper, E.M., 2017. The effect of liquid
1072 composition on the partitioning of Ni between olivine and silicate melt. *Contrib. to Mineral. Petrol.*
1073 172, 3. <https://doi.org/10.1007/s00410-016-1319-8>
- 1074 Moskovitz, N., Gaidos, E., 2011. Differentiation of planetesimals and the thermal consequences of
1075 melt migration. *Meteorit. Planet. Sci.* 46, 903–918. [https://doi.org/10.1111/j.1945-
1076 5100.2011.01201.x](https://doi.org/10.1111/j.1945-5100.2011.01201.x)
- 1077 Néri, A., Guignard, J., Monnereau, M., Bystricky, M., Perrillat, J.-P., Andraut, D., King, A., Guignot, N.,
1078 Tenailleau, C., Duployer, B., Toplis, M.J., Quitté, G., 2020. Reevaluation of metal
1079 interconnectivity in a partially molten silicate matrix using 3D microtomography. *Phys. Earth
1080 Planet. Inter.* 106571. <https://doi.org/10.1016/j.pepi.2020.106571>
- 1081 Néri, A., Guignard, J., Monnereau, M., Toplis, M.J.J., Quitté, G., 2019. Metal segregation in
1082 planetesimals: Constraints from experimentally determined interfacial energies. *Earth Planet.
1083 Sci. Lett.* 518, 40–52. <https://doi.org/10.1016/j.epsl.2019.04.049>
- 1084 O'Neill, H.S.C., Pownceby, M.I., 1993. Thermodynamic data from redox reactions at high
1085 temperatures. I. An experimental and theoretical assessment of the electrochemical method
1086 using stabilized zirconia electrolytes, with revised values for the Fe-"FeO", Co-CoO, Ni-NiO and

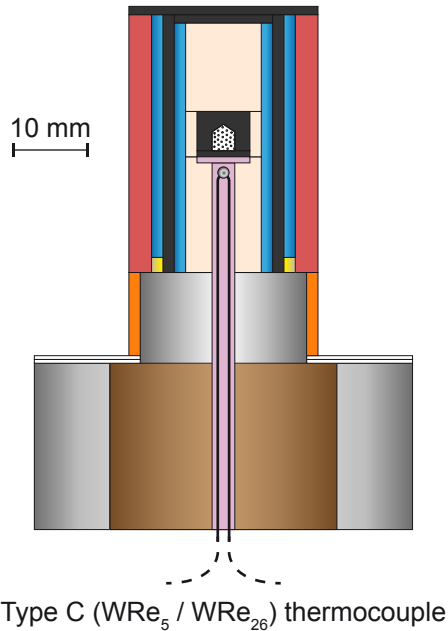
- 1087 Cu-Cu₂O oxygen buffer. *Contrib. to Mineral. Petrol.* 114, 296–314.
1088 <https://doi.org/10.1007/BF01046533>
- 1089 Petry, C., Chakraborty, S., Palme, H., 2004. Experimental determination of Ni diffusion coefficients in
1090 olivine and their dependence on temperature, composition, oxygen fugacity, and crystallographic
1091 orientation. *Geochim. Cosmochim. Acta* 68, 4179–4188.
1092 <https://doi.org/10.1016/j.gca.2004.02.024>
- 1093 Presnall, D.C., Dixon, S.A., Dixon, J.R., O'Donnell, T.H., Brenner, N.L., Schrock, R.L., Dycus, D.W.,
1094 1978. Liquidus phase relations on the join diopside-forsterite-anorthite from 1 atm to 20 kbar:
1095 Their bearing on the generation and crystallization of basaltic magma. *Contrib. to Mineral. Petrol.*
1096 66, 203–220. <https://doi.org/10.1007/BF00372159>
- 1097 Rubie, D.C., 2015. *Formation of the Earth's Core*, Treatise on Geophysics. Elsevier B.V.
1098 <https://doi.org/10.1016/B978-0-444-53802-4.00154-8>
- 1099 Rubie, D.C., Melosh, H.J., Reid, J.E., Liebske, C., Richter, K., 2003. Mechanisms of metal-silicate
1100 equilibration in the terrestrial magma ocean. *Earth Planet. Sci. Lett.* 205, 239–255.
1101 [https://doi.org/10.1016/S0012-821X\(02\)01044-0](https://doi.org/10.1016/S0012-821X(02)01044-0)
- 1102 Rugel, G., Faestermann, T., Knie, K., Korschinek, G., Poutivtsev, M., Schumann, D., Kivel, N.,
1103 Günther-Leopold, I., Weinreich, R., Wohlmuther, M., 2009. New measurement of the Fe60 half-
1104 life. *Phys. Rev. Lett.* 103, 14–17. <https://doi.org/10.1103/PhysRevLett.103.072502>
- 1105 Schindelin, J., Arganda-Carreras, I., Frise, E., Kaynig, V., Longair, M., Pietzsch, T., Preibisch, S.,
1106 Rueden, C., Saalfeld, S., Schmid, B., Tinevez, J.-Y., White, D.J., Hartenstein, V., Eliceiri, K.,
1107 Tomancak, P., Cardona, A., 2012. Fiji: an open-source platform for biological-image analysis.
1108 *Nat. Methods* 9, 676–682. <https://doi.org/10.1038/nmeth.2019>
- 1109 Scott, T., Kohlstedt, D.L., 2006. The effect of large melt fraction on the deformation behavior of
1110 peridotite. *Earth Planet. Sci. Lett.* 246, 177–187. <https://doi.org/10.1016/j.epsl.2006.04.027>
- 1111 Solferino, G.F.D., Thomson, P., Hier-majumder, S., 2020. Pore Network Modeling of Core Forming
1112 Melts in Planetesimals 8, 1–15. <https://doi.org/10.3389/feart.2020.00339>
- 1113 Stone, H.A., Bentley, B.J., Leal, L.G., 1986. An experimental study of transient effects in the breakup
1114 of viscous drops. *J. Fluid Mech.* 173, 131–158. <https://doi.org/10.1017/S0022112086001118>
- 1115 Strong, H.M., Bundy, F.P., 1959. Fusion Curves of Four Group VIII Metals to 100 000 Atmospheres.
1116 *Phys. Rev.* 115, 278–284. <https://doi.org/10.1103/PhysRev.115.278>
- 1117 Taylor, G.J., 1992. Core formation in asteroids. *J. Geophys. Res.* 97, 14717.
1118 <https://doi.org/10.1029/92JE01501>
- 1119 Tomotika, S., 1936. Breaking up of a drop of viscous liquid immersed in another viscous fluid which is
1120 extending at a uniform rate. *Proc. R. Soc. London. Ser. A - Math. Phys. Sci.* 153, 302–318.
1121 <https://doi.org/10.1098/rspa.1936.0003>
- 1122 Toplis, M.J., Mizzon, H., Monnereau, M., Forni, O., Mccsween, H.Y., Mittlefehldt, D.W., McCoy, T.J.,
1123 Prettyman, T.H., De Sanctis, M.C., Raymond, C.A., Russell, C.T., 2013. Chondritic models of 4
1124 Vesta: Implications for geochemical and geophysical properties. *Meteorit. Planet. Sci.* 48, 2300–
1125 2315. <https://doi.org/10.1111/maps.12195>
- 1126 Vigneresse, J.L., Barbey, P., Cuney, M., 1996. Rheological transitions during partial melting and
1127 crystallization with application to felsic magma segregation and transfer. *J. Petrol.* 37, 1579–
1128 1600. <https://doi.org/10.1093/petrology/37.6.1579>
- 1129 Wasson, J.T., Kallemeyn, G.W., 1988. Compositions of Chondrites. *Philos. Trans. R. Soc. A Math.*
1130 *Phys. Eng. Sci.* 325, 535–544. <https://doi.org/10.1098/rsta.1988.0066>
- 1131 Weisberg, M.K., McCoy, T.J., Krot, A.N., 2006. Systematics and Evaluation of Meteorite Classification,
1132 in: Lauretta, D.S., McSween, H.Y. (Eds.), *Meteorites and the Early Solar System II*. University of
1133 Arizona Press, pp. 19–52.
- 1134 Yao, Z., Mungall, J.E., 2020. Flotation mechanism of sulphide melt on vapour bubbles in partially
1135 molten magmatic systems. *Earth Planet. Sci. Lett.* 542, 116298.
1136 <https://doi.org/10.1016/j.epsl.2020.116298>
- 1137 Yoshino, T., Walter, M.J., Katsura, T., 2003. Core formation in planetesimals triggered by permeable
1138 flow. *Nature* 422, 154–157. <https://doi.org/10.1038/nature01459>

1139 Yoshino, T., Watson, E.B., 2005. Growth kinetics of FeS melt in partially molten peridotite: An analog
1140 for core-forming processes. *Earth Planet. Sci. Lett.* 235, 453–468.
1141 <https://doi.org/10.1016/j.epsl.2005.04.021>
1142

Type S Pt / PtRh₁₀ thermocouple



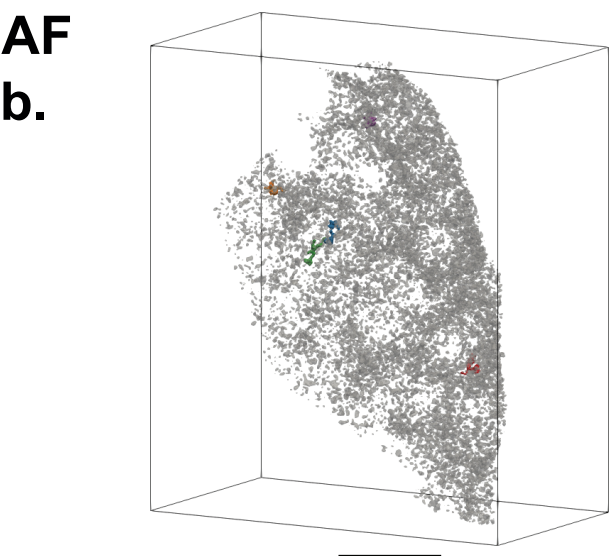
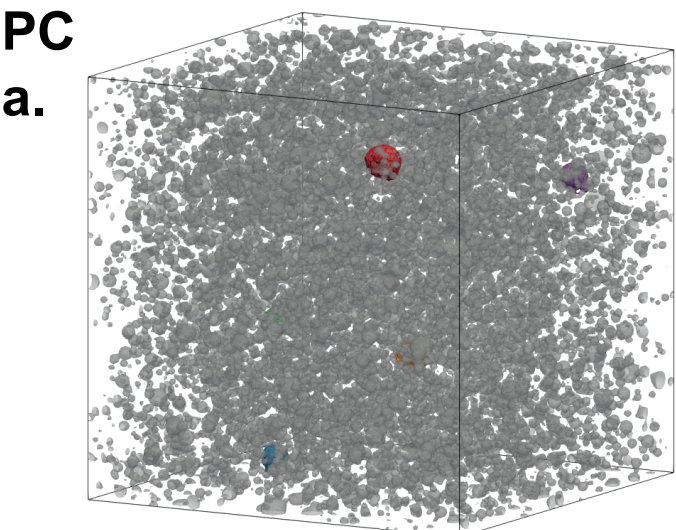
a. Atmosphere furnace assembly



b. Piston-cylinder assembly

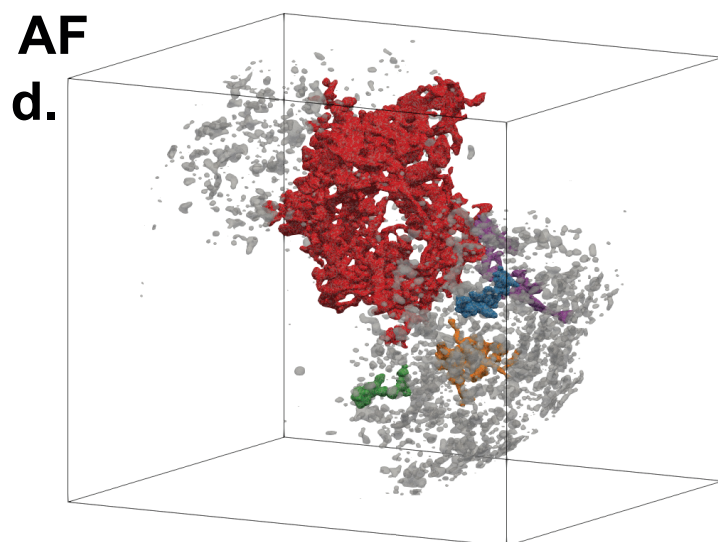
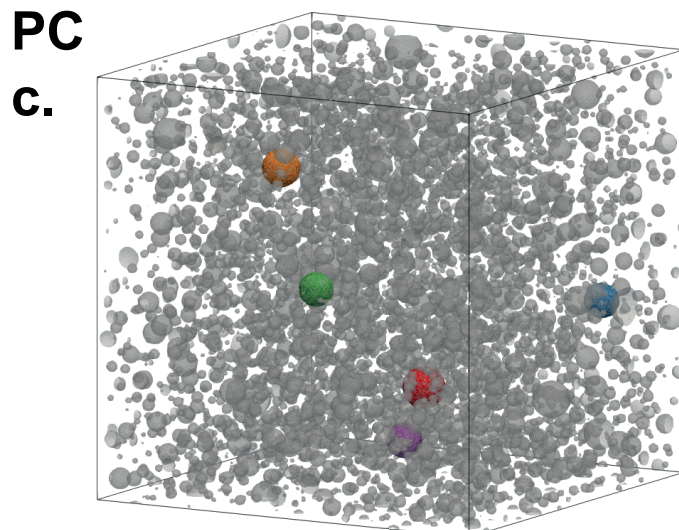
- MgO
- Sample
- Graphite
- Al₂O₃
- Pyrex
- Brass ring
- NaCl cell
- Pyrophyllite ring
- Plastic foils
- Steel pieces
- Tungsten carbide

$\langle 62.5 : 32.5 : 5 \rangle$

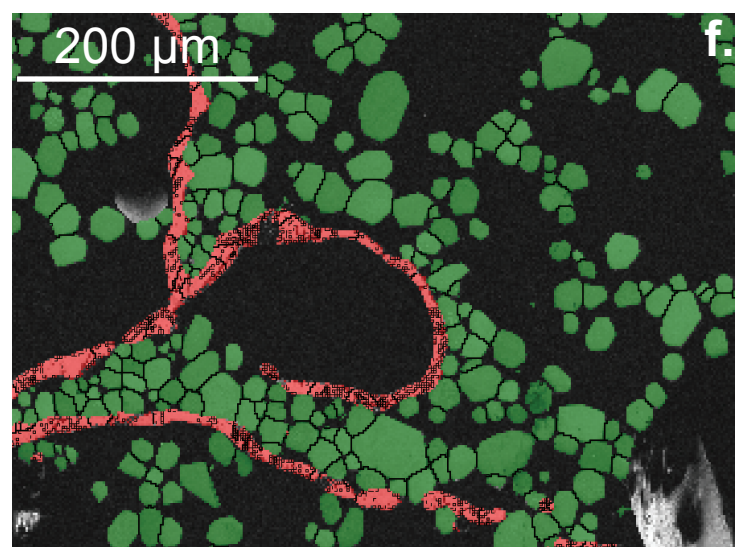
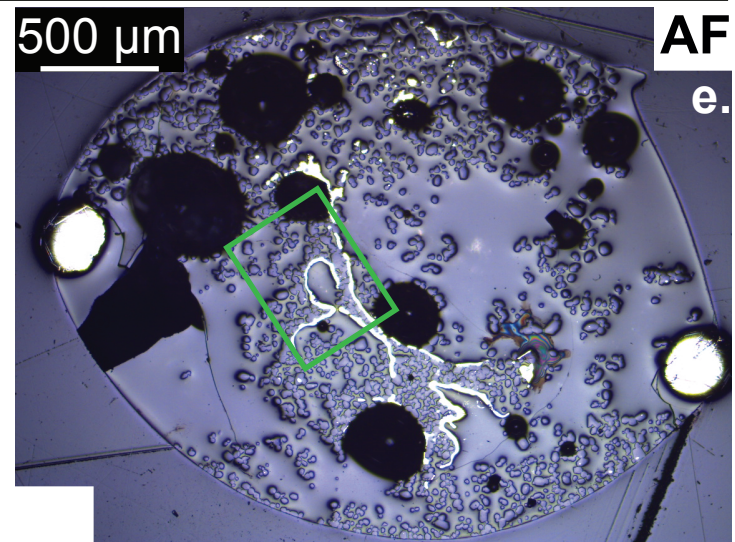


1st 2nd 3rd 4th 5th
largest blobs

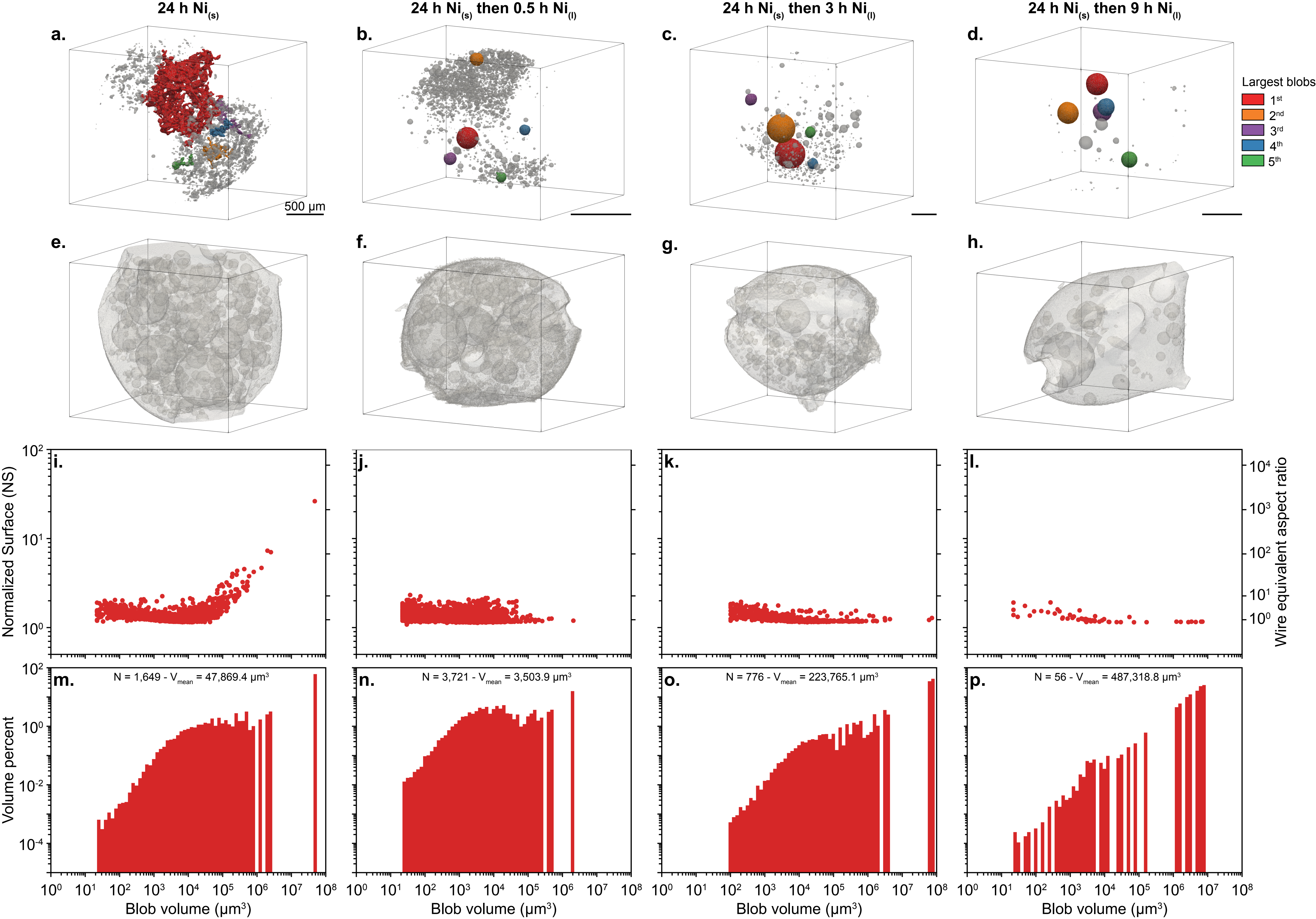
$\langle 20 : 75 : 5 \rangle$



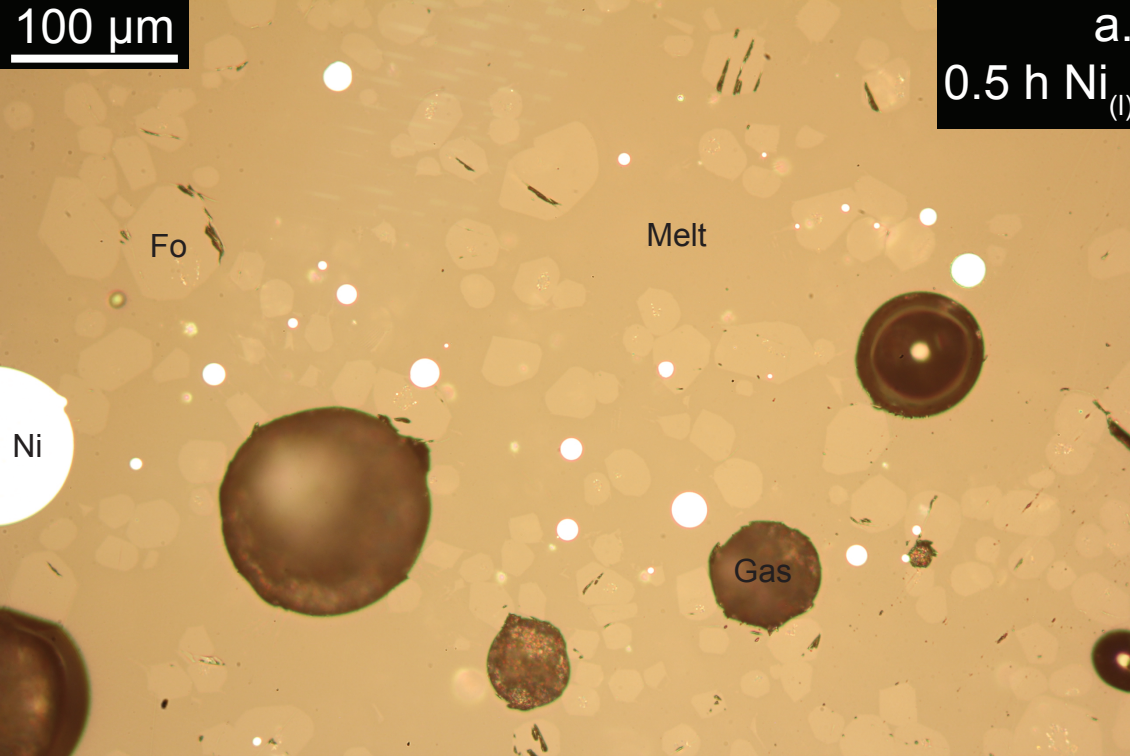
500 μm



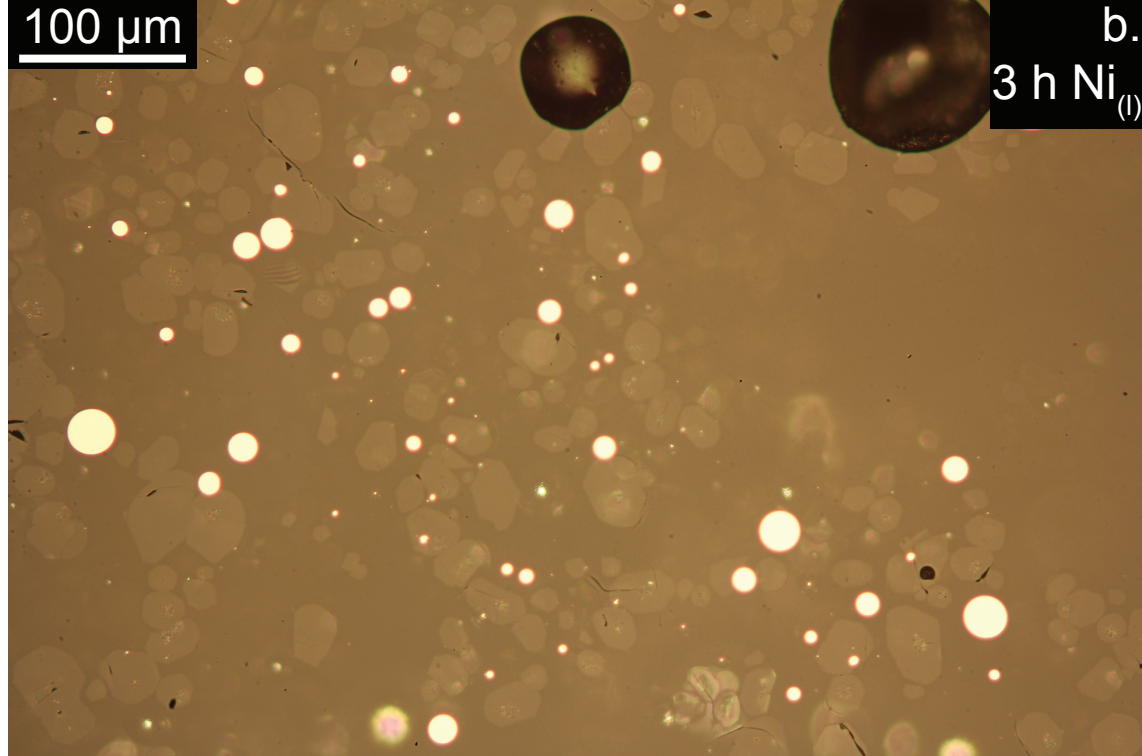
Nickel
Forsterite



100 μm



100 μm



100 μm

